SCISPACE
formerly Typeset

Open access • Journal Article • DOI:10.1021/ACSAMI.8B18153

Highly Electroactive Ni Pyrophosphate/Pt Catalyst toward Hydrogen Evolution Reaction. — Source link

Jayaraman Theerthagiri, Eduardo S. F. Cardoso, Guilherme V. Fortunato, Gleison A. Casagrande ...+3 more authors

Institutions: Sathyabama University, Federal University of Mato Grosso do Sul, Indian Institute of Science, Thiruvalluvar University

Published on: 09 Jan 2019 - ACS Applied Materials & Interfaces (American Chemical Society)

Topics: Nickel, Water splitting, Catalysis, Pyrophosphate and Ascorbic acid

Related papers:

- Fundamental aspects and recent advances in transition metal nitrides as electrocatalysts for hydrogen evolution reaction: A review
- Developments and perspectives of oxide-based catalysts for the oxygen evolution reaction
- Benchmarking Heterogeneous Electrocatalysts for the Oxygen Evolution Reaction
- Recent advances in transition metal phosphide nanomaterials: synthesis and applications in hydrogen evolution reaction
- Precision and correctness in the evaluation of electrocatalytic water splitting: revisiting activity parameters with a critical assessment

Share this paper:

View more about this paper here: https://typeset.io/papers/highly-electroactive-ni-pyrophosphate-pt-catalyst-toward-3og26f68r5

ACS APPLIED MATERIALS & INTERFACES

Research Article

Cite This: ACS Appl. Mater. Interfaces 2019, 11, 4969−4982

www.acsami.org

Highly Electroactive Ni Pyrophosphate/Pt Catalyst toward Hydrogen Evolution Reaction

Jayaraman Theerthagiri,[‡,†] Eduardo S. F. Cardoso,[§,†] Guilherme V. Fortunato,[§,†] Gleison A. Casagrande,[§] Baskar Senthilkumar,[∥] Jagannathan Madhavan,[⊥] and Gilberto Maia*[,§]

[‡]Centre of Excellence for Energy Research, Sathyabama Institute of Science and Technology (Deemed to be University), Chennai 600119, India

[§]Institute of Chemistry, Universidade Federal de Mato Grosso do Sul, Senador Filinto Muller Avenue, 1555, Campo Grande, Mato Grosso do Sul 79074-460, Brazil

[∥]Materials Research Centre, Indian Institute of Science, Bangalore 560012, India

[⊥]Solar Energy Lab, Department of Chemistry, Thiruvalluvar University, Vellore 632115, Tamil Nadu, India

Supporting Information

ABSTRACT: Robust electrocatalysts toward the resourceful and sustainable generation of hydrogen by splitting of water via electrocatalytic hydrogen evolution reaction (HER) are a prerequisite to realize high-efficiency energy research. Highly electroactive catalysts for hydrogen production with ultralow loading of platinum (Pt) have been under exhaustive exploration to make them cutting-edge and cost-effectively reasonable for water splitting. Herein, we report the synthesis of hierarchically structured nickel pyrophosphate (β-$Ni_2P_2O_7$) by a precipitation method and nickel phosphate ($Ni_3(PO_4)_2$) by two different synthetic routes, namely, simple cost-effective precipitation and solution combustion processes. Thereafter, Pt-decorated nickel pyrophosphate and nickel phosphate (β-$Ni_2P_2O_7$/Pt and $Ni_3(PO_4)_2$/Pt) were prepared by using potassium hexachloroplatinate and ascorbic acid. The fabricated novel nickel pyrophosphate and nickel phosphate/Pt materials were utilized as potential and affordable electrocatalysts for HER by water splitting. The detailed electrochemical studies revealed that the β-$Ni_2P_2O_7$/Pt (1 $\mu g \cdot cm^{-2}$ Pt) electrocatalyst showed excellent electrocatalytic performances for HER in acidic solution with an overpotential of 28 mV at −10 $mA \cdot cm^{-2}$, a Tafel slope of 32 mV·dec, and an exchange current density (j_0) of −1.31 $mA \cdot cm^{-2}$, which were close to the values obtained using the Vulcan/Pt (8.0 $\mu g \cdot cm^{-2}$ Pt), commercial benchmarking electrocatalyst with eight times higher Pt amount. Furthermore, the β-$Ni_2P_2O_7$/Pt electrocatalyst maintains an excellent stability for over −0.1 V versus RHE for 12 days, keeping j_0 equal after the stability test (−1.28 mA cm^{-2}). Very well-distributed Pt NPs inside the "cages" on the β-$Ni_2P_2O_7$ structure with a crystalline pattern of 0.67 nm distance to the $Ni_2P_2O_7$/Pt electrocatalyst, helping the Volmer−Tafel mechanism with the Tafel reaction as a major rate-limiting step, help to liberate very fast the Pt sites after HER. The high electrocatalytic performance and remarkable durability showed the β-$Ni_2P_2O_7$/Pt material to be a promising cost-effective electrocatalyst for hydrogen production.

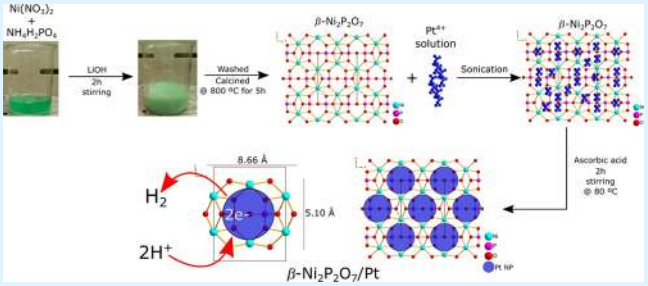

KEYWORDS: *hydrogen evolution reaction, nickel, phosphate, platinum, pyrophosphate*

INTRODUCTION

Hydrogen (H_2) is the cleanest energy transporter to the hydrogen-based economy and has gained an increasing attention as a substitute for fossil fuels. Resourceful and sustainable generation of H_2 is crucial for a hydrogen economy to diminish our reliance on fossil fuels and their harmful environmental impacts.[1−3] Commercially, the generation of H_2 is obtained from methane steam reforming and gasification of coal. However, these two methods have ecological consequences as well as engaged with more cost, which stimulated an extensive attempt to explore clean energy sources. In this pursuit, the sustainable production of H_2 by splitting of water via electrocatalytic hydrogen evolution reaction (HER) has fascinated significant attention because of its characteristics such as low cost, easy fabrication process, high efficiency, environmental friendly, carbon free, and large scale production.[4−6] In the electrocatalytic HER, protons and electrons are combined to generate H_2, being catalyzed by electrochemically active catalysts, with a high current density at a low overpotential.[7] Commonly, platinum is the most extensively utilized electrocatalyst for HER in acid media because of its high stability, low Gibbs free energy (ΔG_H*) for H_2 adsorption, and superior electrocatalytic performances. However, noble Pt strongly hinders its broad commercialization for

Received: October 17, 2018
Accepted: January 9, 2019
Published: January 9, 2019

Downloaded via INDIAN INST OF SCIENCE on March 2, 2019 at 17:53:11 (UTC).
See https://pubs.acs.org/sharingguidelines for options on how to legitimately share published articles.

 © 2019 American Chemical Society

DOI: 10.1021/acsami.8b18153
ACS Appl. Mater. Interfaces 2019, 11, 4969−4982

the large scale H_2 generation because of its high price and little abundance in earth. Thus, this prompted the development of advanced alternative electrocatalysts for HER with cost-effectiveness and also the maintenance of high electrocatalytic performances toward the production of H_2.

More recently, nickel-based electrocatalysts such as nickel phosphide,[8] nickel sulfide,[9] nickel selenide,[10] Ni-MoC_x/carbon black,[11] and Ni@$Ni(OH)_2$/Pd/rGO[12] have been utilized for H_2 production in acidic media. However, none of other catalyst has achieved an HER activity attained from Pt-based electrocatalysts. In this context, researchers made an alternative solution to this standoff, which was to search substitute electrocatalysts by minimizing the dosage of platinum.[13−16] For example, Wang et al.[17] developed $Ni(OH)_2$-supported Pt/C electrocatalysis for H_2 production. The Pt/$Ni(OH)_2$ hybrids could significantly enhance the activity of a pure Pt electrocatalyst for HER performance. In addition, the transition metal hydroxides exhibited good adsorption capabilities for OH^-, produced after the dissociation of water by creating OH^- and H^+. Rapid adsorption of OH^- results in rapid desorption of OH^- from the surface of Pt, which would be used further to enhance the activity of HER performance. Another report by Zheng[18] investigated the electrocatalytic activity of $PtNi_x$ by alteration of stoichiometric ratio of Pt/Ni. As a result, the maximized electrocatalytic performances were achieved for $PtNi_5$ composition toward the HER activity. On the basis of the H_2 adsorption theory, the ΔG_H* value of Ni is closer to zero when compared with Mo, Co, W, and so forth, as a result the alloying of Pt and Ni is predictable to enhance the electrocatalytic behavior toward HER.

In this work, we have synthesized hierarchically structured β-$Ni_2P_2O_7$, $Ni_3(PO_4)_2$, and $Ni_3(PO_4)_2'$ by simple cost-effective methods such as precipitation and solution combustion methods, respectively. In a second step, we have developed Pt-assisted β-$Ni_2P_2O_7$, $Ni_3(PO_4)_2$, and $Ni_3(PO_4)_2'$ composites (β-$Ni_2P_2O_7$/Pt, $Ni_3(PO_4)_2$/Pt, and $Ni_3(PO_4)_2'$/Pt) as advanced electrocatalysts for the H_2 production. To the best of our knowledge and to the extent advancement in this field concerned, this is the first time report on Pt-assisted nickel pyrophosphate and nickel phosphate as electrocatalysts toward HER activity. This present study will display a high electrocatalytic HER activity from low amount of Pt (see Table S1 in Supporting Information for a fast overview/comparison with different materials reported in the literature)[4,6,8,13,14,19−31] and contribute to an advancement of superior electrocatalysts with low cost for H_2 production. The appealing results obtained in materials characterization and electrocatalytic performances are systematically highlighted.

■ EXPERIMENTAL SECTION

Reagents and Instruments. The precursor solutions and metal salts utilized nickel nitrate hexahydrate ($Ni(NO_3)_2.6H_2O$), ammonium dihydrogen phosphate ($NH_4H_2PO_4$), lithium hydroxide (LiOH), sodium hydroxide pellets (NaOH) and urea (NH_2CONH_2) were purchased from Sigma-Aldrich. Potassium hexachloroplatinate (K_2PtCl_6), ascorbic acid (AA), sulfuric acid (H_2SO_4), and $CuSO_4 \cdot 5H_2O$ were obtained from Vetec, and 20% Pt on Vulcan XC72 (20 wt % loading Pt/Vulcan, named Vulcan/Pt) was purchased from Sigma-Aldrich. All reagents utilized in this investigation were used as received.

A typical three-electrode setup of the glass cell used during voltammetric and chronoamperometric measurements contains the following: working electrode, a Teflon-embedded glassy carbon (GC) disk (0.196 cm^2 in geometric area) or a Teflon-embedded Pt disk (0.164 cm^2 in geometric area) (Pine Research Instrumentation) or a carbon paper HCP030N (1.0 cm^2) or a carbon graphite plate (1.0 cm^2); reference electrode, RHE; and counter electrode, a carbon paper HCP030N (3.5 cm^2).

Synthesis of Nickel Pyrophosphate by Precipitation Process. Nickel pyrophosphate (β-$Ni_2P_2O_7$) was synthesized by easy and low-cost precipitation process. For an instance, calculated stoichiometric quantity of $Ni(NO_3)_2 \cdot 6H_2O$ (1.08 mol) and $NH_4H_2PO_4$ (1 mol) was dissolved in 50 mL of distilled water. Then, 30 mL of LiOH (2 mol) solution was introduced dropwise as a precipitating agent under constant magnetic stirring. The resulting mixture was stirred well for overnight in a magnetic stirrer. The final precipitate was collected by centrifugation and washed several times with distilled water.[32] Then, the obtained sample was calcined at 800 °C for 5 h (Scheme S1).

Synthesis of Nickel Phosphate by Precipitation Process. For the synthesis of nickel phosphate ($Ni_3(PO_4)_2$), the calculated stoichiometric quantity of $Ni(NO_3)_2 \cdot 6H_2O$ (3 mol) and $NH_4H_2PO_4$ (2 mol) was uniformly dissolved in 50 mL of double-distilled water, and the pH of the reaction mixture was adjusted to 7 by using 1 M NaOH. The obtained reaction mixture was magnetically stirred for about 5 h. After the completion of the reaction, the acquired precipitate was washed several times using deionized water and then dried at 80 °C for overnight. Finally, the obtained product was calcined at 700 °C for 5 h.

Synthesis of Nickel Phosphate by Solution Combustion Process. Nickel phosphate ($Ni_3(PO_4)_2'$) was synthesized by a simple solution combustion process. For the synthesis, 4.37 g of $Ni(NO_3)_2 \cdot 6H_2O$ and 1.70 g of $NH_4H_2PO_4$ were dissolved in double-distilled water and followed by the addition of NH_2CONH_2. Urea was used as fuel. All precursor materials were thoroughly dissolved using double-distilled water (20 mL) with constant magnetic stirring to obtain homogenous solution. Then, the obtained reaction mixture was kept on hot plate at 200 °C for dehydration. After complete dehydration, the resulting solid was transferred to a muffle furnace and heat-treated around 300 °C. After 10 min, the decomposition with gradual release of gases was observed. The final foamy product was collected after grinding it on an agate mortar pestle and used for further characterization. The foamy product was calcined at 800 °C for 5h.

The synthesized materials were denoted in this study as nickel pyrophosphate (β-$Ni_2P_2O_7$) "precipitation", nickel phosphate ($Ni_3(PO_4)_2$) "precipitation", and nickel phosphate ($Ni_3(PO_4)_2'$) "solution combustion".

Syntheses of β-$Ni_2P_2O_7$/Pt, $Ni_3(PO_4)_2$/Pt, $Ni_3(PO_4)_2'$/Pt, and Pt Nanoparticles (Pt NPs). Initially, in a beaker, 10 mg of β-$Ni_2P_2O_7$ (or $Ni_3(PO_4)_2$ or $Ni_3(PO_4)_2'$) and 1.56 mg of K_2PtCl_6 (or 0.78 mg of K_2PtCl_6 or 0.39 mg of K_2PtCl_6 only to β-$Ni_2P_2O_7$) or only 1.56 mg of K_2PtCl_6 were mixed with 20 mL of Milli-Q water; then, the reaction mixture was sonicated for at least 20 min. Posteriorly, the dispersion was heated to 80 °C on a hotplate under constant magnetic stirring. When the temperature reached 80 °C, 2.65 mg (or 1.33 or 0.6 mg when was the case) of ascorbic acid was added (solubilized in 1 mL of Milli-Q water) to reduce the Pt ions, and the stirring and heating were maintained for 2 h (the synthesis is resumed in Scheme S1 and Figure S1). After this time, the synthesis was naturally cooled to ambient temperature, rinsed (with Milli-Q water) by centrifugation (at 4500 rpm) five times to remove any residual reactant, and finally the material was dried in an oven at 40 °C.

Fabrication of Electrodes. Initially, the alumina slurries with 1 and 0.05 μm mesh were used for the polishing GC disk, subsequently cleaned by consecutive ultrasonication in Milli-Q water and acetone for 5 min in each solvent. Finally, the cleaned GC disk was subjected to 10 cycles at a scan speed of 50 $mV \cdot s^{-1}$ in the potential range of 0.05−1.2 V. The Pt disk was undertaken for 200 cycles at a scan rate of 900 $mV \cdot s^{-1}$ in the potential range of 0.05−1.2 V. The N_2-saturated 0.5 M H_2SO_4 was changed several times as required to make sure a clean surface of both GC and Pt electrodes. The carbon paper HCP030N and carbon graphite plate were cleaned by ultrasonication in several Milli-Q water and followed by two cycles at a scan speed of 50 $mV \cdot s^{-1}$ in a potential window of 0.05−1.2 V at N_2-saturated 0.5 M

DOI: 10.1021/acsami.8b18153
ACS Appl. Mater. Interfaces 2019, 11, 4969−4982

H_2SO_4 solution. The catalyst inks were prepared by sonication of 0.5 mg of different catalysts (β-$Ni_2P_2O_7$, $Ni_3(PO_4)_2$, $Ni_3(PO_4)_2'$, β-$Ni_2P_2O_7$/Pt, $Ni_3(PO_4)_2$/Pt, $Ni_3(PO_4)_2'$/Pt, or Vulcan/Pt) at 1 mL of Milli-Q water during at least 1 h. Additionally, a catalyst ink was prepared by sonication of 0.15 mg of Pt NPs at 10 mL of Milli-Q water during at least 1 h. A homogeneous thin film was consequently produced by dripping 16 μL of an aqueous solution of β-$Ni_2P_2O_7$, $Ni_3(PO_4)_2$, $Ni_3(PO_4)_2'$, β-$Ni_2P_2O_7$/Pt, $Ni_3(PO_4)_2$/Pt, $Ni_3(PO_4)_2'$/Pt, Vulcan/Pt at 0.5 mg·mL^{-1} (loading: 40 μg·cm^{-2}) or Pt NPs at 0.015 mg·mL^{-1} (loading: 1.2 μg·cm^{-2}) onto the GC disk surface and allowing it to dry at ambient temperature. The fabricated electrodes were then connected in a three electrode electrochemical cell setup containing a 0.5 M H_2SO_4 solution saturated with N_2 or H_2 (both obtained from White Martins with 5.0 purity).

Apparatuses and Measurements. The structural crystalline phase identification of the developed β-$Ni_2P_2O_7$, $Ni_3(PO_4)_2$, $Ni_3(PO_4)_2'$, and β-$Ni_2P_2O_7$/Pt samples (15−30 mg) was recorded by powder X-ray diffraction (XRD) technique via a Siemens D5000, Diffrac Plus XRD Commander, X-ray diffractometer with Cu Kα radiation (λ = 0.154 nm) at a scan rate of 0.01 °·s^{-1}. The structural morphology of the synthesized samples was inspected by field emission scanning electron microscopy (FE-SEM) with an FEI Quanta 250 microscope system.

β-$Ni_2P_2O_7$, β-$Ni_2P_2O_7$/Pt, and β-$Ni_2P_2O_7$/Pt after the 12th day structures were characterized by transmission electron microscopy (TEM), performed on a JEOL JEM2100 LaB_6 apparatus operating at 200 kV. For this, diluted β-$Ni_2P_2O_7$, β-$Ni_2P_2O_7$/Pt, and β-$Ni_2P_2O_7$/Pt after the 12th day aqueous reaction solutions were dropped onto carbon films embedded on a lacey carbon film on a 400-mesh copper grid (Ted Pella).

The electron energy loss spectroscopy (EELS) experiments were performed using a JEOL JEM 2100F microscope (operated at 200 kV) equipped with a GATAN Imaging Filtering system (EELS-GIF Tridium). All EEL spectra were collected with a dispersion of 0.3 eV/ch, with an aperture label of 2.0 mm under an STEM illumination mode. The software Digital Micrograph was used to subtract the background (through the power law method).

XPS analysis was performed with an Omicron surface analysis station equipped with an SPHERA hemispherical analyzer and a DAR 400 Al Kα (1486.7 eV) X-ray source. The chamber was evacuated to 1×10^{-8} mbar during analysis. Pass energies were 50 and 10 eV for survey- and high-resolution spectra, respectively. The Voigt-type function with Gaussian (70%) and Lorentzian (30%) was used for the deconvolution of XPS spectra.

ICP-OES was performed to identify the content of Pt in β-$Ni_2P_2O_7$/Pt using Thermo Fisher Scientific iCAP 6300 Duo equipment with the operating conditions of RF power being 1250 W, sample flow was 0.45 L·min^{-1}, plasma gas flow rate was 12 L·min^{-1}, an integration time of 5 s, a stabilization time of 20 s, nebulization pressure was 20 psi, and axial view mode, λ = 214.423 nm to Pt). Further, more detail on the Pt ICP-OES identification can be seen in Supporting Information.

All electrochemical techniques such as cyclic voltammogram (CV), chronoamperometry, hydrodynamic CV, and hydrodynamic linear potential scan (HLS) were measured by an AFP2 WaveDriver 20 bipotentiostat−galvanostat equipped with an AFMSRCE modulated speed rotator (Pine Research Instrumentation).

A PGSTAT128N potentiostat−galvanostat (Autolab) equipped with a FRA2.X module was utilized for EIS measurements, which was carried out at a fixed OCP value of around 0.55 V (on average) or at −10, −20, and −50 mV in 0.5 M H_2SO_4, with potential perturbation of 10 mV (rms) within a frequency range of 10 mHz to 100 kHz. Concern was taken to make sure that AC impedance output data matched to the interfaces being inspected at high frequencies, as depicted in ref 33. Every HLS curve was adjusted for ohmic drop resistance estimated and determined from the fitted intercept at high frequency of EIS. Ohmic drop resistance estimated in 0.5 M H_2SO_4 was 6 Ω on average (Figure S2).

Normalization of HLS curves was based on electrochemically active surface area (ECSA) and actual electrode geometric area values. The ECSA values were obtained by stripping of H_{upd} (50 mV·s^{-1}) and Cu_{upd}.[34,35] Charge density was taken as 210 μC·cm^{-2} [36] for bare Pt and Vulcan/Pt/GC-modified electrode surfaces and 420 μC·cm^{-2} for the β-$Ni_2P_2O_7$/Pt surface. Cu_{upd} stripping was carried out in 1 mM $CuSO_4$ in 0.5 M H_2SO_4 solution. The potential at the β-$Ni_2P_2O_7$/Pt/GC electrode was kept at 1.0 V during 200 s, followed by a 900 s step at 0.4 V, and consequently by an HLS from 0.4 to 1.0 V at 5 mV·s^{-1} and 600 rpm.

The ECSA was also estimated from the electrochemical double-layer capacitance (C_{dl}) to β-$Ni_2P_2O_7$ and β-$Ni_2P_2O_7$/Pt by collecting CVs from 5 to 800 mV·s^{-1} in a potential window of 0.1 V centered at the OCP (measured currents in this non-Faradaic potential region might be because of the double-layer charging).[37] During these CV measurements, the working electrode was held at each potential vertex for 10 s before beginning the next sweep.[37] The double-layer charging current is equal to the product of the potential scan rate, ν, and the C_{dl},[37] expressed by eq 1:

$$\Delta I/2 = (I_{(+)} - I_{(-)})/2 = \nu \times C_{dl} \quad (1)$$

The ECSA based on the C_{dl} was calculated according to eq 2

$$\mathrm{ECSA} = C_{dl}/C_s \quad (2)$$

where C_s is the specific capacitance, here, we used the capacitance of an atomically smooth planar surface of the material per unit area under identical electrolyte conditions with a value of 0.035 mF·cm^{-2}.[37]

RESULTS AND DISCUSSION

XRD Studies. The XRD patterns of the produced β-$Ni_2P_2O_7$/Pt, β-$Ni_2P_2O_7$, $Ni_3(PO_4)_2$, and $Ni_3(PO_4)_2'$ materials are depicted in Figure 1. The XRD pattern of synthesized β-

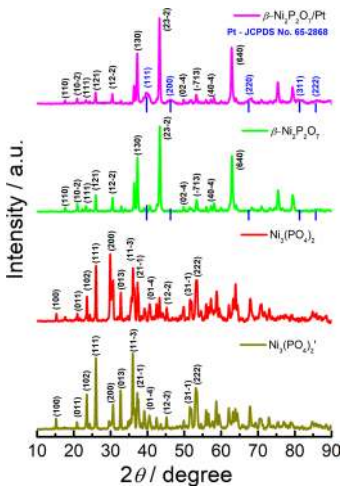

Figure 1. XRD spectra of β-$Ni_2P_2O_7$/Pt, β-$Ni_2P_2O_7$, $Ni_3(PO_4)_2$, and $Ni_3(PO_4)_2'$ samples.

$Ni_2P_2O_7$ by a simple precipitation method is in good agreement with the equivalent (110), (10−2), (111), (121), (12−2), (130), (23−2), (02−4), (−713), (40−4), and (640) diffraction planes of monoclinic $Ni_2P_2O_7$ (JCPDS No. 74-1604). The XRD pattern for β-$Ni_2P_2O_7$/Pt shows the diffraction peaks corresponding to the β-$Ni_2P_2O_7$ sample, in addition to the diffraction peaks for Pt (111), (200), (220), (311), and (222) planes at 2θ = 39.7, 46.3, 67.8, 82.0 and 85.6° (more evident: 39.7 and 46.3°; due to addition of the very small amount of Pt (∼3 wt %) in the sample), respectively, identified for Pt (JCPDS No. 65-2868). The diffraction peaks of the $Ni_3(PO_4)_2$ synthesized by precipitation process revealed several peaks and the exhibited (hkl)

DOI: 10.1021/acsami.8b18153
ACS Appl. Mater. Interfaces 2019, 11, 4969−4982

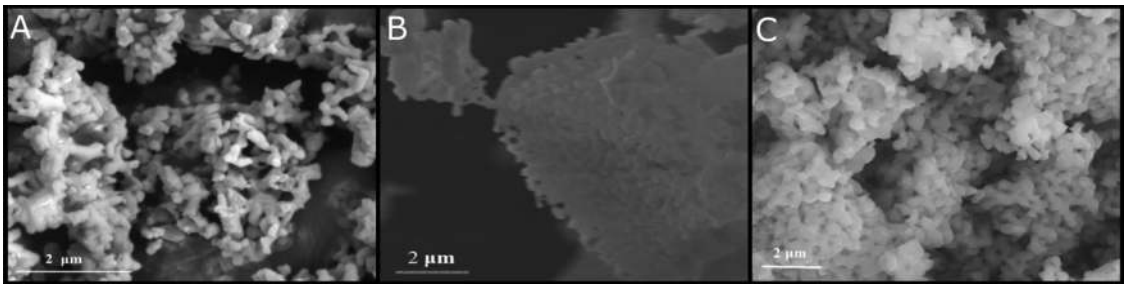

Figure 2. FE-SEM morphology of (A) β-$Ni_2P_2O_7$, (B) $Ni_3(PO_4)_2$, and (C) $Ni_3(PO_4)_2'$ samples.

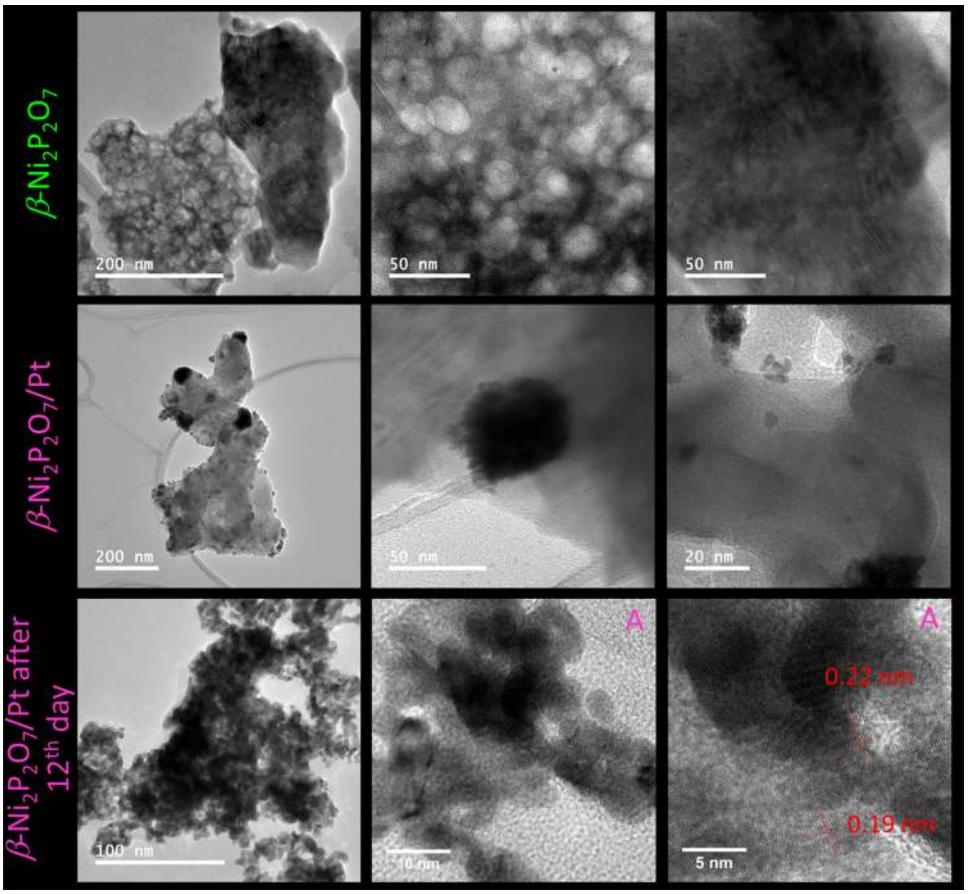

Figure 3. TEM images of β-$Ni_2P_2O_7$, β-$Ni_2P_2O_7$/Pt, and β-$Ni_2P_2O_7$/Pt after the 12th day samples, and HR-TEM images of (A) β-$Ni_2P_2O_7$/Pt after the 12th day sample.

diffraction planes (100), (011), (102), (111), (200), (013), (11-3), (21-1), (01-4), (12-2), (31-1), and (222). They are indexed according to the information of monoclinic crystal structure of $Ni_3(PO_4)_2$ (JCPDS No. 15-3160). The diffraction pattern of $Ni_3(PO_4)_2'$ synthesized by solution combustion process illustrates that the diffraction pattern of $Ni_3(PO_4)_2$ synthesized by precipitation route is not changed by the synthetic route. However, it could be noticed that the small changes in diffraction angles and peak intensity, which might be due to the various synthetic conditions on $Ni_3(PO_4)_2$ generating substantial expansion and contraction of the lattice constants.

The above XRD investigation confirms the formation of β-$Ni_2P_2O_7$, β-$Ni_2P_2O_7$/Pt, $Ni_3(PO_4)_2$, and $Ni_3(PO_4)_2'$ materials, and the resultant average crystalline size calculated using Scherrer's equation[38−40] was about 9.1, 8.9, 36.6, and 41.8 nm, respectively. The difference in the average crystalline size of $Ni_3(PO_4)_2$ and $Ni_3(PO_4)_2'$ by changing of synthetic conditions and the biggest change in crystalline size to β-$Ni_2P_2O_7$ in relation to $Ni_3(PO_4)_2$ and $Ni_3(PO_4)_2'$ could be noticed, in addition to the decreased crystalline size to β-$Ni_2P_2O_7$/Pt in relation to β-$Ni_2P_2O_7$. The smaller crystalline size may be likely to show an enhanced electrocatalytic active sites, which may also lead to show an improved electrocatalytic performance.

Morphology Studies. The shape and structural morphologies of the synthesized β-$Ni_2P_2O_7$, $Ni_3(PO_4)_2$, and $Ni_3(PO_4)_2'$ samples were analyzed by FE-SEM, and the resulting pictures are exhibited in Figure 2. The FE-SEM morphology of the β-$Ni_2P_2O_7$ sample shows an aggregated granular-like[32] particles (Figure 2A). However, the FE-SEM image of $Ni_3(PO_4)_2$ shows a micrometer size granular-like surface structure made by nanoflakes (Figure 2B). The structural morphology of $Ni_3(PO_4)_2'$ synthesized by precipitation process exhibited the hierarchical granular-like

DOI: 10.1021/acsami.8b18153
ACS Appl. Mater. Interfaces 2019, 11, 4969−4982

morphology (Figure 2C). It was observed that the structural morphology of $Ni_3(PO_4)_2$ sample is tightly packed granular-like particles, which are probable to be an additional benefit for the transport of electron.[41,42] However, the particles such as the β-$Ni_2P_2O_7$ sample may be better arranged at a GC surface.

Further, the structures of β-$Ni_2P_2O_7$, β-$Ni_2P_2O_7$/Pt, and Pt NP samples were investigated by TEM, HR-TEM, electron diffraction pattern, HAADF-STEM, and EDX mapping images; the equivalent pictures are shown in Figures 3 and 4 and Figures S3 and S4. The TEM images of β-$Ni_2P_2O_7$ (Figure 3 and Figure S3) show rounded whitish structures with different sizes as well as darkened structures such as plates[32] with a distance of fringes of 0.97 nm. β-$Ni_2P_2O_7$/Pt has visible, large Pt NPs directly or not directly supported at the β-$Ni_2P_2O_7$ structure (Figure 3 and Figure S3) as well as small Pt NPs also appearing to be imbibed into the β-$Ni_2P_2O_7$ structure, presenting a mean Pt particle size distribution (PSD) of 9.7 ± 4.6 nm (Figure S3). The distance of fringes is now 0.67 nm. These distances of fringes are close to distances present in the unitary cell of β-$Ni_2P_2O_7$ structure (Scheme S1). TEM and HR-TEM images of Pt NPs synthesized in the absence of β-$Ni_2P_2O_7$ are shown in Figure S4, which can be seen larger Pt NPs such as the large Pt NPs directly or not directly supported at β-$Ni_2P_2O_7$ structure (Figure 3 and Figure S3), with Pt dendritic structures[43−47] (Figure S4). The visible distance of fringes appeared now as 0.19 to 0.22 nm (HR-TEM image A at Figure S4 to Pt NPs).

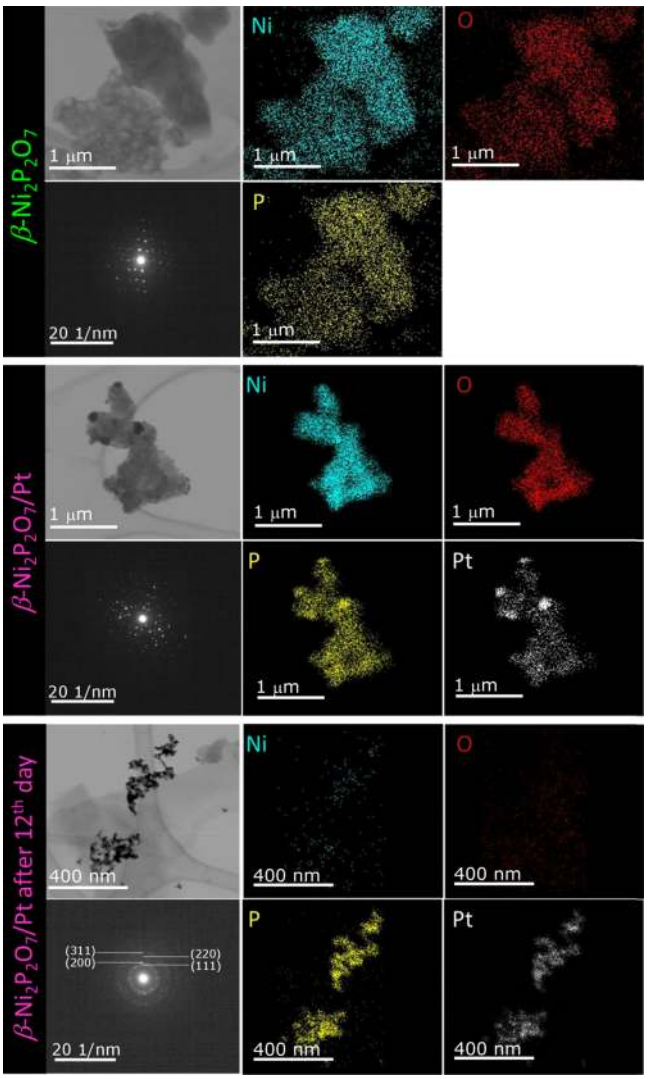

Figure 4. HAADF-STEM, EDX mapping, and electron diffraction pattern images of β-$Ni_2P_2O_7$, β-$Ni_2P_2O_7$/Pt, and β-$Ni_2P_2O_7$/Pt after the 12th day samples.

The EDX mapping (Figure 4) to the β-$Ni_2P_2O_7$ sample shows clearly the presence of Ni, O, and P, equally distributed[32] and very close to each other in the rounded whitish and plate structures of β-$Ni_2P_2O_7$. The diffraction pattern is well visible to β-$Ni_2P_2O_7$ sample (Figure 4). To the β-$Ni_2P_2O_7$/Pt sample, the EDX mapping (Figure 4) to Ni, O, and P is similar to the β-$Ni_2P_2O_7$ sample with exception to the detection of Pt very well distributed to β-$Ni_2P_2O_7$ and closer to the P atoms, which reinforces the occurrence of small Pt NPs imbibed into the β-$Ni_2P_2O_7$ structure (see high intensity of detected Pt to larger Pt NPs at β-$Ni_2P_2O_7$/Pt sample in Figure 4). The diffraction pattern is also well visible to β-$Ni_2P_2O_7$/Pt sample (Figure 4); however, it appears different when compared with the diffraction pattern to β-$Ni_2P_2O_7$, as previous detected to different distance of fringes to β-$Ni_2P_2O_7$ and β-$Ni_2P_2O_7$/Pt (TEM images at Figure 3). The diffraction pattern to Pt NP samples (Figure S4) is consistent with the spots in distances matching to face-centered cubic (fcc) crystalline phase of Pt with (111), (200), (220), and (311) planes.[43−47] The low intensity of the spots (Figure S4) is consistent with the Pt dendritic structures.[43−47] The β-$Ni_2P_2O_7$/Pt sample (Figure 4) presents not well-defined concentric spot characteristic of Pt NPs (Figure S4), which was not identified at the β-$Ni_2P_2O_7$ sample (Figure 4).

EELS Analysis. The Ni $L_{2,3}$ edge electron energy loss near-edge structures (ELNES), core-loss spectra in the EELS, of $Ni(NO_3)_2$ (standard), β-$Ni_2P_2O_7$, and β-$Ni_2P_2O_7$/Pt are shown in Figure 5A. Spin-orbit coupling to Ni-2p orbitals emerges as doubly degenerated $2p_{1/2}$ and quadruple $2p_{3/2}$.[48] The main transitions should be from Ni-2p levels to Ni-3d.[48] Thereby, the Ni $L_{2,3}$ edge ELNES for different samples (Figure 5A) comprises two major peaks related for transitions from $2p_{1/2}$ (L_2 edge around 872 eV) and from $2p_{3/2}$ orbitals (L_3 edge around 855 eV), in agreement with results shown for NiO.[48] For $Ni(NO_3)_2$ (standard), the experimental L_3 peak at 855 eV was not completely sharp in addition to present a shoulder toward lower energy, and the L_2 peak at 871.5 eV was trapezoidal shaped. For β-$Ni_2P_2O_7$, the L_3 peak at 855 eV was totally sharp in addition to present a shoulder toward higher energy, presenting also a triangular-shaped L_2 peak at 872 eV. For β-$Ni_2P_2O_7$/Pt, the L_3 peak at 855 eV was broad, presenting also a triangular-shaped L_2 peak at 872 eV. The profile of the Ni $L_{2,3}$ edge ELNES firmly reflects the nearby electronic structure of the Ni atom, for instance, spin state, oxidation, and coordination number.[48] The distinctive features of the Ni $L_{2,3}$ edge ELNES, as a result, propose that the Ni atoms are in a different electronic structure in $Ni(NO_3)_2$ (standard), β-$Ni_2P_2O_7$, and β-$Ni_2P_2O_7$/Pt.

The O−K edge ELNES mostly matched to electron transitions from O 1s core level to unoccupied O 2p orbitals.[48] The ELNES of $Ni(NO_3)_2$ (standard) (Figure 5B) consists of four major peaks at 525, 528, 537.7 (with shoulders at low and high energy, the main peak), and 562 eV. The ELNES of β-$Ni_2P_2O_7$ (Figure 5B) consists of only two major peaks. The first peak is coincident with the third (including the shoulders) and the fourth peaks of $Ni(NO_3)_2$ (standard) at 537.3 and 563.5 eV, respectively, to β-$Ni_2P_2O_7$. The O−K edge ELNES

DOI: 10.1021/acsami.8b18153
ACS Appl. Mater. Interfaces 2019, 11, 4969−4982

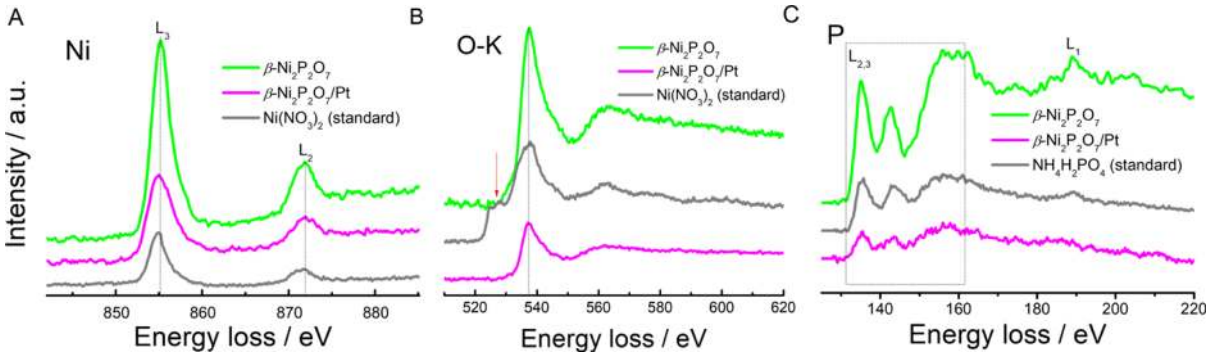

Figure 5. EELS spectra of the (A) Ni-$L_{2,3}$ edge, (B) O−K edge, and (C) P−L edge of the β-$Ni_2P_2O_7$/Pt, β-$Ni_2P_2O_7$, $Ni(NO_3)_2$, and $NH_4H_2PO_4$.

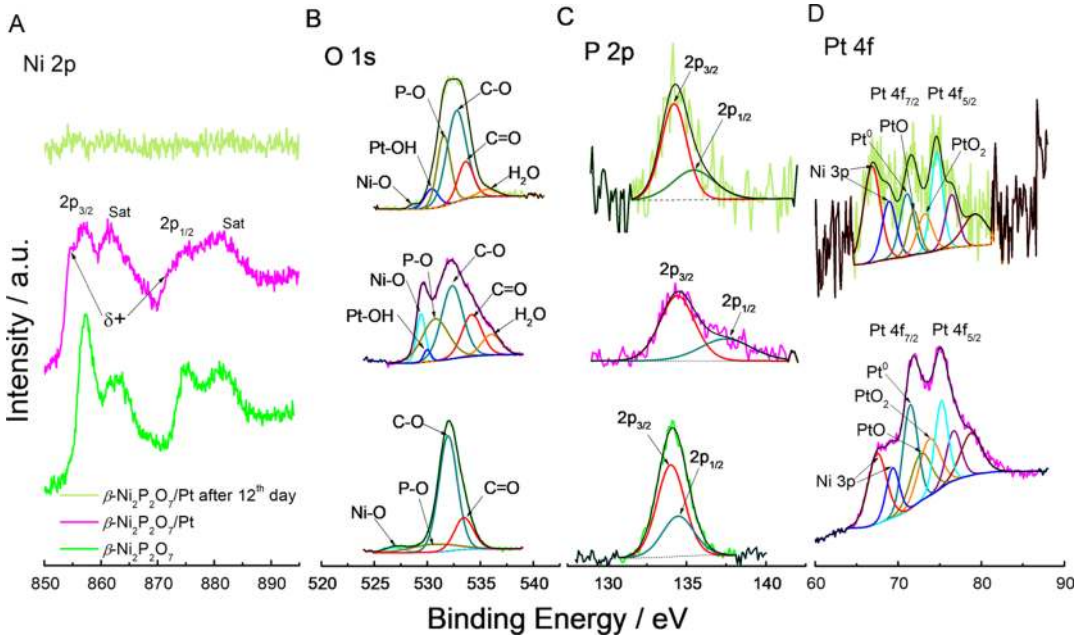

Figure 6. High-resolution (A) Ni 2p, (B) O 1s, (C) P 2p, and (D) Pt 4f XPS spectra of β-$Ni_2P_2O_7$, β-$Ni_2P_2O_7$/Pt, and β-$Ni_2P_2O_7$/Pt after the 12th day.

of β-$Ni_2P_2O_7$/Pt in Figure 5B contains of two major peaks at 537.3 and 562 eV. For the last two materials, the first peak is located at higher energy than that for $Ni(NO_3)_2$ (standard). The electron transitions corresponding to the main peak to different materials may take place via covalent bonding between the O 2p and Ni 3d orbitals,[48] meaning that the disappearance of the peaks at 525 and 528 eV from $Ni(NO_3)_2$ (standard) in relation to β-$Ni_2P_2O_7$, and the disappearance of the shoulders from the peak at 537.3 eV to β-$Ni_2P_2O_7$/Pt in relation to β-$Ni_2P_2O_7$ indicates that the covalent bonding becomes stronger in the order of $Ni(NO_3)_2$ (standard), β-$Ni_2P_2O_7$, and β-$Ni_2P_2O_7$/Pt. This is in agreement with distance of fringes decreased from 0.97 to 0.67 nm to β-$Ni_2P_2O_7$ and β-$Ni_2P_2O_7$/Pt, respectively (TEM images at Figure 3)

The P-$L_{2,3}$ and L_1 edge ELNES correspond to electron transition from P 2p core level to both s- (l = 0) and d-character (l = 2) final states[49] and P 2s core level to p state (l = 1), respectively.[49] The ELNES of $NH_4H_2PO_4$ (standard) (Figure 5C) consists of four major peaks at 135.5, 143.4, 156 (P $L_{2,3}$), and 189.5 (P L_1) eV. The ELNES of β-$Ni_2P_2O_7$ (Figure 5C) consists of similar peaks at 135.2, 142.7, 159.5 (trapezoidal shaped) (P $L_{2,3}$), and 189 (P L_1) eV. The ELNES of β-$Ni_2P_2O_7$/Pt in Figure 5C consists of peaks at 135.4, 144, 157 eV (P $L_{2,3}$), and not identifiable P L_1 peak. The peak around 136 eV is attributed to P_xO_y species,[50,51] as well the peaks from 140 to 160 eV (and the peak at 189 eV).[51] The presence of Ni at β-$Ni_2P_2O_7$ displaced the peaks in ELNES spectrum to low energy in comparison with the ELNES of $NH_4H_2PO_4$ (standard). The presence of Pt at β-$Ni_2P_2O_7$/Pt displaced the peaks in ELNES spectrum to high energy in comparison with the ELNES of β-$Ni_2P_2O_7$, with not identifiable P L_1 peak to β-$Ni_2P_2O_7$/Pt—most probable due to the few unfilled p states and their energy distribution is broad than that of the d states, so the L_1 turns invisible.[49] This observation is corroborated by the presence of Pt NPs close to the P atoms to β-$Ni_2P_2O_7$/Pt sample (Figure 4). The slight but perceptible differences in FTIR spectra (Figure S5) are also experimental evidence of the interactions of small amount of Pt (Pt NPs) present in the β-$Ni_2P_2O_7$/Pt material, which in turn affect the vibrational modes of the P−O−P groupments (see complementary information in the Supporting Information about FTIR analysis).

XPS Analysis. Figure S6 depicts the XPS spectra of β-$Ni_2P_2O_7$ and β-$Ni_2P_2O_7$/Pt where Ni 2p, O 1s, C 1s, P 2s, P 2p, and Ni 3p, in addition to Pt 4s, Pt 4d, and Pt 4f (Pt peaks to β-$Ni_2P_2O_7$/Pt) peaks are noticeable. Positions and atomic

DOI: 10.1021/acsami.8b18153
ACS Appl. Mater. Interfaces 2019, 11, 4969−4982

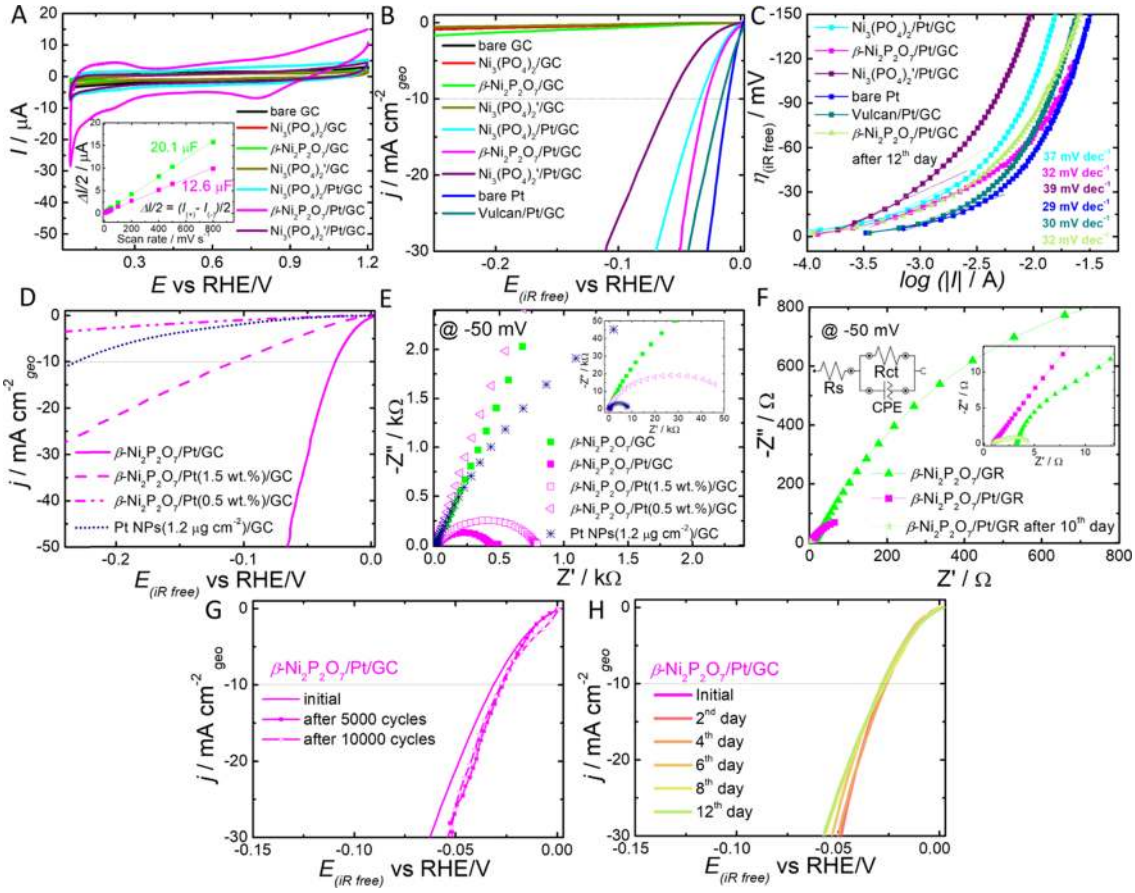

Figure 7. (A) CVs for bare and modified GC electrodes. Potential scan rate: 50 mV·s^{-1}. Potential scan starts at 1.2 V. Inset: $\Delta I/2$ vs ν for modified GC electrodes. (B) HLSs (corrected for ohmic-drop resistance) recorded with bare Pt and GC and modified GC electrodes. Scans started at 0.0 V. ω = 1600 rpm, ν: 5 mV·s^{-1}. Current densities (currents used from Figure S7C) shown by electrode geometric area. (C) Tafel plots for bare Pt and modified GC electrodes (data from Figure S7C). (D) HLSs (corrected for ohmic-drop resistance) recorded with modified GC electrodes. Scans started at 0.0 V. ω = 1600 rpm, ν: 5 mV·s^{-1}. Current densities shown by electrode geometric area. Plane impedance plots for (E) modified GC and (F) GR electrodes. Potential perturbation: 10 mV (rms). Frequency range: 100 kHz−10 mHz. Constant potential for EIS acquisition: −50 mV vs RHE. Inset in (E): plane impedance plots extended to 50 kΩ. Inset in (F): plane impedance plots contracted to 15 Ω. HLSs (corrected for ohmic-drop resistance) for GC electrode modified with the β-$Ni_2P_2O_7$/Pt electrocatalyst before and after (G) the stability test (10000 cycles between 0.0 and −0.1 V at 50 mV·s^{-1}) and (H) chronoamperometric experiment (potential jumped from 0 to -0.1 V vs RHE and kept at -0.1 V vs RHE for 12 days, Figure S12). ω = 1600 rpm; scan rate: 5 mV·s^{-1}. Scans started at 0.00 V. Current densities shown by electrode geometric area. The results were obtained in H_2-saturated 0.5 M H_2SO_4 solution with exception to inset of Figure 7A that was obtained in N_2-saturated 0.5 M H_2SO_4 solution.

and mass percentages (Table S5) were obtained from the XPS spectrum in Figure S6.

The β-$Ni_2P_2O_7$ surface analysis from the XPS measurement (Figure S6) shows mass percentages of Ni (54%) and P (46%) (Table S5). However, to β-$Ni_2P_2O_7$/Pt, the surface analysis from the XPS measurement (Figure S6) shows mass percentages of Ni (72.7%), P (20%), and Pt (7.3%) (Table S5). The carbon and oxygen were not quantified because their contributions are totally from the graphite (GR) support surface to carbon and mixed contribution of support and the β-$Ni_2P_2O_7$/Pt and β-$Ni_2P_2O_7$/Pt surfaces to oxygen. The films of β-$Ni_2P_2O_7$ and β-$Ni_2P_2O_7$ on the GR surface did not have enough thickness to avoid the support surface contribution to XPS responses. However, even considering relative percentages (not including carbon and oxygen), Ni mass percentage is high than P as expected to β-$Ni_2P_2O_7$ mass percentage composition as well as Pt mass percentage is lower than the Ni mass percentage and close to that determined by ICP-OES to β-$Ni_2P_2O_7$/Pt mass percentage composition (see below).

The deconvoluted high-resolution Ni 2p XPS spectrum (Figure 6A) contains two peaks at 857.3 and 875.2 eV with their respective satellites shakeup at 862.5 and 880.9 eV corresponding to the $2p_{3/2}$ and $2p_{1/2}$ levels, respectively, in a 2:1 ratio (Table S6). A spin-orbital splitting of 18 eV between the peaks and the presence of satellites peaks indicates that Ni^{2+} species[32,52−55] are present at the β-$Ni_2P_2O_7$ surface. In addition, the β-$Ni_2P_2O_7$/Pt surface revealed two shoulders at 854.4 (Ni $2p_{3/2}$ δ+) and 872.2 (Ni $2p_{1/2}$ δ+) with small % content (Figure 6A and Table S6) characteristic of a small amount of Pt in direct "contact" to Ni^{2+} species. These HR-XPS spectra are narrowly connected to the EELS spectra in Figure 5A.

The deconvoluted O 1s HR-XPS spectrum (Figure 6B) to β-$Ni_2P_2O_7$ (there is a small peak in addition to a broad peak without deconvolution) assigned to Ni−O (526.9 eV), P−O−P (530.6 eV),[53,54] C−O (532.0 eV), and C═O (533.5 eV) groups, with large % content of the last two groups (Table S6) because of the large contribution of the GR surface. To the β-$Ni_2P_2O_7$/Pt surface (very broad two peaks without deconvolution are visible), in addition, there is clearly a new peak assigned to Pt−OH (530.0 eV) group (Figure 6B) with small % content (Table S6), as expected due to the small amount of

DOI: 10.1021/acsami.8b18153
ACS Appl. Mater. Interfaces 2019, 11, 4969−4982

Pt present at β-$Ni_2P_2O_7$/Pt (see ICP-OES result below). These HR-XPS spectra maintain close relationship to the EELS spectra in Figure 5B.

The deconvoluted P 2p HR-XPS spectrum (Figure 6C) to β-$Ni_2P_2O_7$ (there is a broad peak without deconvolution) has been correlated to P $2p_{3/2}$ (134.0 eV) and P $2p_{1/2}$ (134.5 eV) peaks with 2/1 ratio of % content for the first in relation to the second (Table S6), indicating a +5 state for P atoms[52−55] in β-$Ni_2P_2O_7$. To the β-$Ni_2P_2O_7$/Pt surface (there are a broad peak followed by a shoulder without deconvolution), the peaks have been correlated to P $2p_{3/2}$ (134.4 eV) and P $2p_{1/2}$ (137.5 eV) also with 2/1 ratio of % content for the first in relation to the second (Table S6), indicating also +5 state for P atoms[52−55] in β-$Ni_2P_2O_7$/Pt. However, the displacement of P $2p_{1/2}$ peak from 134.5 to 137.5 eV is an evidence of Pt in direct "contact" to P^{5+} species. These HR-XPS spectra maintain close relationship to the EELS spectra in Figure 5C.

Finally, the deconvoluted Pt 4f HR-XPS spectrum (Figure 6D) to β-$Ni_2P_2O_7$/Pt revealed two peaks attributed to Ni $3p_{3/2}$ (67.5 eV) and Ni $3p_{1/2}$ (69.4 eV), in addition to three couples (two spin-orbit split (7/2, 5/2) Pt 4f peaks) of spin-orbit components (Pt $4f_{7/2}$ and Pt $4f_{5/2}$) with fixed separation (3.3 eV) and a relative content ratio of 1.33.[46] The main Pt $4f_{7/2}$ component is located at 71.5 eV and matches to metallic Pt[46] with % content of 32% considering the two spin-orbit split.[46] The another two components were attributed to PtO (72.8 eV) and PtO_2 (73.8 eV)[46] (Table S6). The relatively high amount of Pt^{2+} and Pt^{4+} can originate from synthesis of the electrocatalyst in the presence of oxygen and further contact with oxygen during washing and storage.[46] Definitely, we have metallic Pt NPs in direct "contact" with Ni^{2+} species in the β-$Ni_2P_2O_7$/Pt structure positioned inside the "cages" of β-$Ni_2P_2O_7$ (Scheme S1) and in direct "contact" with Ni^{2+} and P^{5+} species present in the β-$Ni_2P_2O_7$ structure.

ICP-OES Analysis. To definitively confirm the Pt amount present in the β-$Ni_2P_2O_7$/Pt sample, ICP-OES investigation was carried out. The Pt content (% mass/mass) was examined by ICP-OES with obtainable value of 2.98 ± 0.04.

Electrochemical Profile. Figure 7A and Figures S7A,B and S8A−C show the cyclic voltammetric profiles of bare GC, bare Pt, $Ni_3(PO_4)_2$, β-$Ni_2P_2O_7$, $Ni_3(PO_4)_2'$, $Ni_3(PO_4)_2$/Pt, β-$Ni_2P_2O_7$/Pt, $Ni_3(PO_4)_2'$/Pt, and 20 wt % loading Pt/Vulcan supported on the GC surface ($Ni_3(PO_4)_2$/GC, β-$Ni_2P_2O_7$/GC, $Ni_3(PO_4)_2'$/GC, $Ni_3(PO_4)_2$/Pt/GC, β-$Ni_2P_2O_7$/Pt/GC, $Ni_3(PO_4)_2'$/Pt/GC, and Vulcan/Pt/GC-modified electrodes).

The bare GC, $Ni_3(PO_4)_2$/GC, β-$Ni_2P_2O_7$/GC, and $Ni_3(PO_4)_2'$/GC-modified electrodes show only capacitive current behavior in the entire potential window (Figure 7A and Figure S8A). However, for β-$Ni_2P_2O_7$/Pt/GC, it is more evident the region of adsorption/desorption of hydrogen in the potential window of 0.05 to 0.4 V (Figure 7A, Figures S7A and S8A,B) (peak couples totally evidenced in the bare polycrystalline Pt (Figures S7A and S8B) at 0.12 and 0.26 V) on the Pt surface, the region of double layer (capacitive currents, 0.4 to 0.75 V, Figure 7A, Figures S7A and S8A,B), and the region of Pt oxide formation (and reduction) from 0.74 to 1.2 V (a small Pt oxide reduction peak at 0.76 V, Figure 7A, Figures S7A and S8A,B). For bare polycrystalline Pt (Figures S7A and S8B), the Pt oxide formation is totally visible by the currents from 0.80 to 1.2 V, and the Pt oxide reduction characterized by a pronounced reduction peak at 0.82 V. The amplified currents to the Vulcan/Pt/GC-modified electrode (Figures S7B and S8C) are due to the large capacitive currents from the Vulcan XC72 carbon present at the 20 wt % loading Pt/Vulcan electrocatalyst. The not well defined peak couples at the region of adsorption/desorption of hydrogen to the Vulcan/Pt/GC-modified electrode (Figures S7B and S8C) is related with the dispersion of Pt at Vulcan XC72 carbon. The Pt oxide formation to the Vulcan/Pt/GC-modified electrode (Figures S7B and S8C) is well visible by the large currents from 0.80 to 1.2 V and the Pt oxide reduction characterized by a pronounced reduction peak at 0.76 V. The behavior of $Ni_3(PO_4)_2$/Pt/GC and $Ni_3(PO_4)_2'$/Pt/GC-modified electrodes (Figure 7A and Figure S8A) is similar when compared with the Pt behavior observed at the β-$Ni_2P_2O_7$/Pt/GC-modified electrode, exception to the high currents to the β-$Ni_2P_2O_7$/Pt/GC-modified electrode in relation to the other two. The cyclic voltammetric profiles are very similar in N_2-saturated 0.5 M H_2SO_4 for all these electrodes (Figure S8A−C). Zheng et al.[56] suggested that steady H_2 pressure be preserved during the investigation to attain perfect HER polarization curves although H_2 not being a reactant for HER. This is the justification for our electrochemical experiments to be mainly discussed at H_2-saturated 0.5 M H_2SO_4 solution.

On the basis of responses in Figure 7A and Figures S7A,B, and S8A−C, it is possible to say that bare Pt and Vulcan/Pt/GC-modified electrode present more Pt active sites than the β-$Ni_2P_2O_7$/Pt/GC-modified electrode. To confirm this observation the ECSA values utilized to get current densities were examined from H_{upd}-stripping to bare Pt and Vulcan/Pt/GC-modified electrode (0.28 and 1.48 cm^2, respectively, based on bare Pt and Vulcan/Pt/GC-modified electrode CV responses in Figures S7A,B and S8B,C) and Cu_{upd}-stripping to β-$Ni_2P_2O_7$/Pt/GC-modified electrode measurements (0.12 cm^2, Figure S9). The magenta curve in Figure S9 behaves likewise to those illustrated in Figure 7A, although the dashed black curve in Figure S9 shows an amplified current in comparison with magenta curve in all potential region that can be related to the exclusion of deposited Cu at Pt sites on the β-$Ni_2P_2O_7$/Pt surface.[35]

In addition, ECSA values estimated from C_{dl} (using eqs 1 and 2, CVs from Figure S10, and inclination values from inset in Figure 7A) to β-$Ni_2P_2O_7$/GC and β-$Ni_2P_2O_7$/Pt/GC-modified electrodes were 0.57 and 0.36 cm^2, respectively. The presence of Pt at the β-$Ni_2P_2O_7$/Pt/GC-modified electrode decreased the ECSA values estimated from C_{dl} in comparison with the β-$Ni_2P_2O_7$/GC-modified electrode. The Pt NPs inside the "cages" of β-$Ni_2P_2O_7$ (Scheme S1) decreased the β-$Ni_2P_2O_7$/Pt ECSA.

Evaluation of the Electrocatalytic Activity of Modified $Ni_3(PO_4)_2$/GC, β-$Ni_2P_2O_7$/GC, $Ni_3(PO_4)_2'$/GC, $Ni_3(PO_4)_2$/Pt/GC, β-$Ni_2P_2O_7$/Pt/GC, $Ni_3(PO_4)_2'$/Pt/GC, and Vulcan/Pt/GC Electrodes, and Bare Pt Electrode toward the HER. The HLS responses to bare Pt and GC electrodes and $Ni_3(PO_4)_2$/GC, β-$Ni_2P_2O_7$/GC, $Ni_3(PO_4)_2'$/GC, $Ni_3(PO_4)_2$/Pt/GC, β-$Ni_2P_2O_7$/Pt/GC, $Ni_3(PO_4)_2'$/Pt/GC, and Vulcan/Pt/GC-modified electrodes are shown in Figure 7B and Figures S7C and S8D.

It is worth noting that all electrochemical analyses were carried out by using a carbon paper HCP030N counter electrode instead of Pt counter electrode in line with the finest practices in pursuit of topic in heterogeneous electrocatalysis,[57] because the Pt redeposition onto the working electrode from the Pt counter electrode (dissolution) should be avoided for HER catalysis studies.[57−59] This care was not taken in several papers cited in Table S1. Also, for comparison, the

DOI: 10.1021/acsami.8b18153
ACS Appl. Mater. Interfaces 2019, 11, 4969−4982

commercially available 20 wt % Pt/C (Vulcan/Pt) was used as a benchmarking catalyst , which is considered as a standard.[57]

For bare GC and GC electrodes modified with $Ni_3(PO_4)_2$, β-$Ni_2P_2O_7$, and $Ni_3(PO_4)_2'$ is not possible to see any catalytic effect for HER in the potential window shown in Figure 7B and Figures S7C and S8D. However, to GC electrodes modified with $Ni_3(PO_4)_2$/Pt, β-$Ni_2P_2O_7$/Pt, $Ni_3(PO_4)_2'$/Pt, and Vulcan/Pt and to bare Pt, the high catalytic effect toward HER is clearly evident, mainly to bare Pt, as expected, and also to Vulcan/Pt. The HLS response to the β-$Ni_2P_2O_7$/Pt/GC-modified electrode appears at more positive potentials than to GC electrodes modified with $Ni_3(PO_4)_2$/Pt and $Ni_3(PO_4)_2'$/Pt (see in Figures S7C and S8D the responses shown only in currents). At −10 mA·cm^{-2}, the overpotential to bare Pt was 10 mV, GC electrode modified with Vulcan/Pt was 16 mV, β-$Ni_2P_2O_7$/Pt was 28 mV, $Ni_3(PO_4)_2$/Pt was 33 mV, and $Ni_3(PO_4)_2'$/Pt was 58 mV, and at −20 mA·cm^{-2}, they were 19, 30, 41, 53, and 85 mV, respectively (Figure 7B), considering only the electrode geometric area. However, considering the ECSA based in upd-stripping (Figure S7D), the bare Pt and GC modified with β-$Ni_2P_2O_7$/Pt and Vulcan/Pt had overpotential at −10 mA·cm^{-2} of 16, 20, and 98 mV, respectively, and at −20 mA·cm^{-2} of 30, 32, and 176 mV. The overpotential values to the β-$Ni_2P_2O_7$/Pt/GC-modified electrode were lower than the value to the Vulcan/Pt/GC-modified electrode and very close to bare Pt, considering the ECSA. In general, the overpotential values considering geometric area and ECSA are lower than the values summarized in Table S1. These results are in agreement with the idea that smaller crystalline sizes (β-$Ni_2P_2O_7$ and $Ni_3(PO_4)_2$) result in higher electrocatalytic active surface, which in turn improves the HER electrocatalytic responses, in addition to the decreased distance of fringes from β-$Ni_2P_2O_7$ to β-$Ni_2P_2O_7$/Pt (TEM images in Figure 3), the detection of Pt very well distributed to β-$Ni_2P_2O_7$ and closer to the P atoms, which reinforces the occurrence of small Pt NPs imbibed into the β-$Ni_2P_2O_7$ structure (Figure 4), the presence of Pt at β-$Ni_2P_2O_7$/Pt displacing the peaks in ELNES spectrum to high energy in comparison with the ELNES of β-$Ni_2P_2O_7$, with not identifiable P L_1 peak to β-$Ni_2P_2O_7$/Pt (Figure 5C), and the presence of metallic Pt NPs in direct "contact" with Ni^{2+} species in the β-$Ni_2P_2O_7$/Pt structure (Figure 6D) positioned inside the "cages" of β-$Ni_2P_2O_7$ (Scheme S1) and in direct "contact" with Ni^{2+} and P^{5+} present in the β-$Ni_2P_2O_7$ structure (Figure 6A,C). It is worth noting that the presence of Pt at the β-$Ni_2P_2O_7$/Pt/GC-modified electrode decreased the ECSA values estimated from C_{dl} in comparison with the β-$Ni_2P_2O_7$/GC-modified electrode.

Using ECSA based on upd-stripping to compare the catalysts (bare Pt and GC-modified electrodes with β-$Ni_2P_2O_7$/Pt and Vulcan/Pt) was possible to identify that GC electrode modified with β-$Ni_2P_2O_7$/Pt is an excellent catalyst toward HER (better electrocatalytic behavior when compared with the Vulcan/Pt/GC-modified electrode and close to bare Pt electrode) because the amount of Pt available at GC electrode modified with β-$Ni_2P_2O_7$/Pt is only close to 1.0 μg·cm^{-2}, an almost negligible amount of Pt when compared with a bulk Pt electrode and eight times lower Pt amount (in mass) compared with Vulcan/Pt catalyst, which was used 8.0 μg·cm^{-2} of Pt. The specific ECSA (see eq S1, Supporting Information) to the GC-modified electrode with β-$Ni_2P_2O_7$/Pt was 61 m^2·g_{Pt}^{-1}, close to that reported by Neyerlin et al.[60] using ultralow Pt-loaded electrodes (3 μg·cm^{-2}). In addition, the Pt and β-$Ni_2P_2O_7$ loadings studied in the present work are lower than the loadings reported in Table S1.

By using ECSA estimated from C_{dl} and calculating the specific ECSA (eq S1) to the GC-modified electrode with β-$Ni_2P_2O_7$ and β-$Ni_2P_2O_7$/Pt, we found 7.3 and 4.6 m^2·$g_{catalyst}^{-1}$. These values are coincident with the values of 6−7 m^2·g^{-1} determined by BET method to β-$Ni_2P_2O_7$,[32,61] which Meguerdichian et al.[61] concluded that β-$Ni_2P_2O_7$ is nonporous. Our results of specific ECSA are totally coincident with the decreased distance of fringes detected to β-$Ni_2P_2O_7$/Pt in relation to β-$Ni_2P_2O_7$ catalyst (TEM image in Figure 3) as well as the occurrence of very well-distributed Pt NPs inside the "cages" of the β-$Ni_2P_2O_7$ structure (Scheme S1).

The turnover frequency (TOF) (Figure S7E) was calculated using eqs S2−S4[62] and resulted at values of 154 and 51 s^{-1} based on ECSA obtained from Cu_{upd} stripping and C_{dl}, respectively, at an overpotential of 28 mV (−10 mA·cm^{-2} based on electrode geometric area, Figure 7B). These values are much higher than those reported by Li et al.[62] even considering only our TOF values based on *ECSA* obtained from C_{dl}. It is clear that some species are of constant TOF tendency at log scale at overpotentials higher than 100 mV (Figure S7E). At 100 mV, the TOF values are 1461 and 500 s^{-1} based on ECSA obtained from Cu_{upd} stripping and C_{dl}, respectively.

To understand better the electrocatalytic effect toward HER, the Tafel plots were produced (Figure 7C) using data in Figure S7C.

It is clear that the linear behaviors to Tafel plots in the range of log |*I*| from −4 to −2 and from slope of these Tafel linear behaviors were calculated the "mV·dec^{-1}" (Table 1). Also, for η = 0 from Tafel linear behavior, the exchange current densities (j_0) were obtained (Table 1). The investigation of Tafel slope is an important parameter to expose the principal steps concerned in the mechanism of H_2 evolution on electrocatalysts. Generally, the possible three principal reaction steps are Volmer reaction (eq 3), Heyrovsky reaction (eq 4), and Tafel reaction (eq 5).[2,63,64]

Table 1. Tafel Slopes and Exchange Current Densities from HER for Modified GC Electrodes (Figure 7C)

modified GC electrode	low *I* (mV·dec^{-1})	j_0 (mA·cm^{-2}) (by geometric area)	j_0 (mA·cm^{-2}) (by *ECSA* based on upd-stripping)
$Ni_3(PO_4)_2$/Pt/GC	37	−1.13	
β-$Ni_2P_2O_7$/Pt/GC	32	−1.31	−2.14
β-$Ni_2P_2O_7$/Pt/GC after the 12th day	32	−1.28	−2.09
$Ni_3(PO_4)_2'$/Pt/GC	39	−0.72	
bare Pt	29	−4.22	−2.47
vulcan/Pt/GC	30	−2.73	−0.36

$$H_3O^+ + e^- \rightarrow H_{ads} + H_2O \text{ (RDS: 120 mV)} \quad (3)$$

$$H_3O^+ + H_{ads} + e^- \rightarrow H_2 + H_2O \text{ (RDS: 40 mV)} \quad (4)$$

$$H_{ads} + H_{ads} \rightarrow H_2 \text{ (RDS: 30 mV)} \quad (5)$$

In light of the over three principal reaction steps, two mechanisms, namely, Volmer−Heyrovsky and Volmer−Tafel are probable for HER. As per this point, the bare Pt and the GC-modified electrodes with β-$Ni_2P_2O_7$/Pt and Vulcan/Pt electrocatalysts with lower Tafel slopes (∼30 mV/dec) match

DOI: 10.1021/acsami.8b18153
ACS Appl. Mater. Interfaces 2019, 11, 4969−4982

to the Volmer−Tafel mechanism with Tafel reaction as a major rate limiting step. The GC-modified electrodes with $Ni_3(PO_4)_2$/Pt and $Ni_3(PO_4)_2'$/Pt electrocatalysts showed Tafel slopes of 37−39 mV·dec^{-1} (Table 1), which corresponds to the Volmer−Heyrovsky mechanism with the Heyrovsky reaction as a major rate limiting step. These Tafel slopes are in line or even lower than the values summarized in Table S1.

The value of Tafel slope of 29 mV·dec^{-1} (Table 1) to bare Pt is equal to that one reported in the literature of 30 mV·dec^{-1},[65,66] in addition to j_0 (−4.22 and −2.47 mA·cm^{-2} per electrode geometric area and ECSA based on upd-stripping, respectively), higher than the reported in literature ∼−1.00 mA·cm^{-2}.[65,66] The GC-modified electrodes with $Ni_3(PO_4)_2$/Pt, β-$Ni_2P_2O_7$/Pt, Vulcan/Pt, and $Ni_3(PO_4)_2'$/Pt electrocatalysts showed Tafel slopes in an average of 39 to 30 mV·dec^{-1}, close to the bare Pt, and to GC-modified electrodes with $Ni_3(PO_4)_2$/Pt, β-$Ni_2P_2O_7$/Pt, Vulcan/Pt, and $Ni_3(PO_4)_2'$/Pt electrocatalysts, the j_0 (−1.61 mA·cm^{-2} in average) was lower than that to bare Pt. However, considering the ECSA based on upd-stripping, the j_0 to the GC-modified electrode with the β-$Ni_2P_2O_7$/Pt electrocatalyst was very close to bare Pt and six times higher in comparison with the GC-modified electrode with the Vulcan/Pt electrocatalyst (Table 1).

The GC-modified electrode with the β-$Ni_2P_2O_7$/Pt electrocatalyst presents better results toward HER than that reported by Devadas and Imae[22] to Pt NPs immobilized on graphene oxides, carbon nanohorns, and carbon nanotubes through a dendrimer-mediated chemical reaction, using ∼1 wt % of Pt NPs, and even lower than the values reported in Table S1.

The HER electrocatalytic activity comparisons were made by decreasing systematically the amount of Pt used during the synthesis of β-$Ni_2P_2O_7$/Pt electrocatalysts as well as with Pt NP electrocatalysts in relation to the β-$Ni_2P_2O_7$/Pt (∼1.0 μg·cm^{-2}) electrocatalyst (Figure 7D), and the HER electrocatalysis became worse from the sequence of β-$Ni_2P_2O_7$/Pt (∼0.5 μg·cm^{-2}, 1.5 wt %), Pt NP (1.2 μg·cm^{-2}), and β-$Ni_2P_2O_7$/Pt (∼0.25 μg·cm^{-2}, 0.5 wt %) electrocatalysts. At −10 mA·cm^{-2}, the overpotentials are 28, 111, 232, and 460 mV, respectively (Figure 7D), this considers only the electrode geometric area. Importantly, the Pt NP (1.2 μg·cm^{-2}) electrocatalyst, which had approximately the same amount of Pt as the β-$Ni_2P_2O_7$/Pt (∼1.0 μg·cm^{-2}) electrocatalyst, showed much worse electrocatalysis than β-$Ni_2P_2O_7$/Pt (∼1.0 μg·cm^{-2}), reinforcing the need of very well-distributed Pt NPs inside the "cages" of the β-$Ni_2P_2O_7$ structure (Scheme S1), with the lower limit of Pt amount to the β-$Ni_2P_2O_7$/Pt electrocatalyst to present higher HER activity being found as ∼1.0 μg·cm^{-2}.

EIS experiments in different overpotentials were conducted at GC- and GR-modified electrodes (Figure 7E,F and Figure S11). In an overpotential of 50 mV and GC-modified electrodes (Figure 7E), the resistance to charge transfer (R_{ct}) is enormous to the β-$Ni_2P_2O_7$/GC electrode (∼340 kΩ), ∼50 kΩ to β-$Ni_2P_2O_7$/Pt(∼0.25 μg·cm^{-2}, 0.5 wt %)/GC electrode, and ∼8.4 kΩ to Pt NPs (1.2 μg·cm^{-2})/GC electrode, and improved enough to β-$Ni_2P_2O_7$/Pt(∼0.5 μg·cm^{-2}, 1.5 wt %)/GC electrode (∼780 Ω), and definitively improved to β-$Ni_2P_2O_7$/Pt(∼1 μg·cm^{-2}, 3.0 wt %)/GC electrode (∼500 Ω). In GR-modified electrodes (Figure 7F), the R_{ct} is also high to β-$Ni_2P_2O_7$/GR electrode (higher than 2.7 kΩ) and ∼374 Ω to β-$Ni_2P_2O_7$/Pt(∼1.0 μg·cm^{-2}, 3.0 wt %)/GR electrode. The R_{ct} is decreased, increasing the overpotential from 10 to 50 mV as well as changing from H_2- to N_2-saturated 0.5 M H_2SO_4 solution (Figure S11). The increased overpotential facilitates the charge transfer from the modified electrode to produce H_2 as well as the H_2-saturated 0.5 M H_2SO_4 solution slightly difficult the charge transfer from the modified electrode to produce H_2.

The β-$Ni_2P_2O_7$/Pt(∼1 μg·cm^{-2}, 3.0 wt %)/GC(or GR) electrode presents the most facilitated charge transfer to produce H_2 (Figure 7E,F and Figure S11) because of the ideal synergistic effect between the amount of Pt NPs inside of the β-$Ni_2P_2O_7$ structure and their distribution on the electrode surface.

Electrocatalytic Stability Tests. GC modified with the β-$Ni_2P_2O_7$/Pt electrode was tested for stability in H_2-saturated 0.5 M H_2SO_4 at a potential scan rate of 50 mV·s^{-1} for 10,000 cycles between 0.0 and −0.1 V or keeping constant the potential at −0.1 V (skipping the potential from 0 to −0.1V, chronoamperometric experiment) and following the current with time for 12 days (Figure S12).[67] The GC electrode modified with β-$Ni_2P_2O_7$/Pt was kept in stationary state, and it was not tilted in relation to the electrochemical cell. The chronoamperometric result is shown in Figure S12 in which the case is observed an increase in current densities after each initiated day of chronoamperometric experiment from in average −1.75 until −0.50 mA·cm^{-2} (stable currents) after few hours. This increase in current densities as well as the overall low current densities can be attributed to the GC electrode modified with β-$Ni_2P_2O_7$/Pt being kept in stationary state and not tilted in relation to the electrochemical cell, in addition to the constant production of H_2 macro- (photo in Figure S12), micro-, and nanobubbles blocking the electrocatalytic Pt surface on the β-$Ni_2P_2O_7$/Pt electrocatalyst.

The HLS readings obtained before and after testing are depicted in Figure 7G,H and Figure S11. To GC electrode modified with β-$Ni_2P_2O_7$/Pt, the overpotential decreased by 6% (after 5000 cycles) and remained the same (after 10000 cycles) at −10 mA·cm^{-2} in relation to initial situation (before cycles) and decreased 15% (after 5000 cycles) and 8% (after 10000 cycles) at −20 mA·cm^{-2} in relation to initial situation (Figure 7G). The overpotential remained the same (after the 12th day) at −10 mA·cm^{-2}, and increased 10% (after the 12th day) at −20 mA·cm^{-2} in relation to initial situation (Figure 7H). To GR electrode modified with the β-$Ni_2P_2O_7$/Pt electrocatalyst, the overpotentials are improved after the 12th day to linear potential scan experiments conducted in the presence of N_2- and H_2-saturated 0.5 M H_2SO_4 solution (Figure S11).

The stability of the β-$Ni_2P_2O_7$/Pt electrocatalyst was maintained after 10,000 cycles and after 12 days of chronoamperometric measurements and importantly, at −0.1 V, will present current densities higher than −40 mA·cm^{-2}. The Tafel (Figure 7C) slope to GC electrode modified with the β-$Ni_2P_2O_7$/Pt electrocatalyst after stability test is equal (32 mV·dec^{-1}) to GC electrode modified with the β-$Ni_2P_2O_7$/Pt electrocatalyst before stability test and j_0 is also equal after the stability test (Table 1).

The β-$Ni_2P_2O_7$/Pt electrocatalyst after 12 days of chronoamperometric measurements showed a visible distance of fringes of 0.19−0.22 nm (HR-TEM image A in Figure 3) similar to Pt NPs (HR-TEM image A in Figure S4), mean PSD of 13.7 ± 3.9 nm (Figure S3), revealing some increase in Pt NPs size, EDX mapping with the decreased presence of Ni and O, and the substantial presence of Pt circled by P (Figure 4), in addition to diffraction pattern consistent with the spots in

DOI: 10.1021/acsami.8b18153
ACS Appl. Mater. Interfaces 2019, 11, 4969−4982

distances corresponding to (111), (200), (220), and (311) planes typical of Pt materials with fcc crystalline patterns[43−47] such as Pt NP sample (Figure S4B).

The β-$Ni_2P_2O_7$/Pt electrocatalyst after 12 days of chronoamperometric measurements showed only distinguishable O 1s and C 1s peaks at the XPS spectrum (Figure S6), with total carbon contribution originated from the GR support surface and mixed contribution of support surface and the β-$Ni_2P_2O_7$/Pt electrocatalyst surface after 12 days of chronoamperometric measurements to oxygen. The high-resolution Ni 2p XPS spectrum (Figure 6A) does not evidence the Ni presence on the β-$Ni_2P_2O_7$/Pt electrocatalyst surface because of the accentuated Ni dissolution after 12 days of chronoamperometric measurements. The deconvoluted O 1s HR-XPS spectrum (Figure 6B) to the β-$Ni_2P_2O_7$/Pt electrocatalyst surface after 12 days of chronoamperometric measurements (it is visible a broad peak without deconvolution) presents a peak assigned to Ni−O (528.7 eV) group with very small % content (Table S6) and a peak assigned to Pt−OH (530.5 eV) group (Figure 6B) with high % content (Table S6) in comparison with the β-$Ni_2P_2O_7$/Pt surface (Table S6), revealing a decreased amount of Ni to the β-$Ni_2P_2O_7$/Pt surface after 12 days of chronoamperometric measurements, in accordance with the EDX mapping response (Figure 4). The deconvoluted P 2p HR-XPS spectrum (Figure 6C) to the β-$Ni_2P_2O_7$/Pt surface after 12 days of chronoamperometric measurements (there is a broad peak followed by a small shoulder without deconvolution) has been correlated to P $2p_{3/2}$ (134.3 eV) and P $2p_{1/2}$ (135.5 eV) peaks with 2/1 ratio of % content for the first in relation to the second (Table S6), indicating also +5 state for P atoms.[52−55] The displacement of P $2p_{1/2}$ peak from 137.5 to 135.5 eV (β-$Ni_2P_2O_7$/Pt surface in relation to β-$Ni_2P_2O_7$/Pt surface after 12 days of chronoamperometric measurements) is an evidence of Pt being in direct "contact" to P^{5+} species with decreased "contact" with Ni (the amount of Ni was enough decreased) (see also EDX mapping, Figure 4). Finally, the deconvoluted Pt 4f HR-XPS spectrum (Figure 6D) to the β-$Ni_2P_2O_7$/Pt surface after 12 days of chronoamperometric measurements revealed two peaks attributed to Ni $3p_{3/2}$ (66.9 eV) and Ni $3p_{1/2}$ (68.9 eV), in addition to three couples (two spin-orbit split (7/2, 5/2) Pt 4f peaks) of spin-orbit components (Pt $4f_{7/2}$ and Pt $4f_{5/2}$) with fixed separation (2.9 eV) and a relative content ratio of 0.75. The main Pt $4f_{7/2}$ component is located at 71.1 eV and corresponds to metallic Pt[46] with % content of 29% considering the two spin-orbit split.[46] The other two components were attributed to PtO (71.9 eV) and PtO_2 (73.2 eV)[46] (Table S6). The relatively amount of Pt^{2+} and Pt^{4+} in relation to Pt^0 is not different (comparing the β-$Ni_2P_2O_7$/Pt surface after 12 days of chronoamperometric measurements with the β-$Ni_2P_2O_7$/Pt surface) from the original amount of Pt^{2+} and Pt^{4+} attributed to be originate from synthesis of the electrocatalyst in the presence of oxygen and further contact with oxygen during washing and storage.[46] Definitely, we have metallic Pt NPs in direct "contact" with Ni^{2+} and P^{5+} species present in the β-$Ni_2P_2O_7$/Pt structure after 12 days of chronoamperometric measurements (see also EDX mapping, Figure 4).

Additionally, the GR-modified with the β-$Ni_2P_2O_7$/Pt electrocatalyst after 12 days of chronoamperometric measurements showed decreased R_{ct} to produce H_2 with the increased overpotential and in H_2-saturated 0.5 M H_2SO_4 solution (Figure 7F and Figure S11), with the best result of 5 Ω (very small R_{ct} value).

These combined information reflects—even occurring Ni dissolution and loss of oxygen atoms to β-$Ni_2P_2O_7$/Pt structure—that Pt NPs surrounded (in "contact") by P (in addition to Ni with decreased amount in overall structure) atoms—this ideal combination—very well distributed on the electrode surface, keep high electrocatalytic activity toward HER, inclusive due to the tremendous facility of charge transfer of this combined system to produce H_2.

The impressive HER electrocatalytic efficiency to the β-$Ni_2P_2O_7$/Pt electrocatalyst can be attributed initially to the small crystalline size of β-$Ni_2P_2O_7$ in comparison with $Ni_3(PO_4)_2$ and $Ni_3(PO_4)_2'$. Also, ($Ni_3(PO_4)_2$/Pt is the best HER catalyst than $Ni_3(PO_4)_2'$/Pt, $Ni_3(PO_4)_2$ has lower crystalline size than $Ni_3(PO_4)_2'$, coupled with:

(1) very well-distributed Pt NPs inside of the "cages" on the β-$Ni_2P_2O_7$ structure with a crystalline pattern of 0.67 nm in distance, helping the Volmer−Tafel mechanism—Tafel reaction as a major rate limiting step—to liberate very fast the Pt sites after HER. The GC-modified electrodes with $Ni_3(PO_4)_2$/Pt and $Ni_3(PO_4)_2'$/Pt electrocatalysts showed Tafel slopes corresponding to the Volmer−Heyrovsky mechanism with Heyrovsky reaction as a major rate limiting step, which appears to liberate more slowly the Pt sites after HER.

(2) the synergic effect between Pt and Ni/P (the direct "contact" between metallic Pt NPs with Ni^{2+} and P^{5+} species present in the β-$Ni_2P_2O_7$ structure, facilitating enormously the charge transfer to HER by strongly decreasing the R_{ct} from the β-$Ni_2P_2O_7$ to β-$Ni_2P_2O_7$/Pt catalyst) may decrease the hydrogen adsorption energy at the Pt NP surface, facilitating the liberation of Pt sites during HER, when compared with electrocatalysts involving only Pt (Pt NPs, bare Pt, and Vulcan/Pt).

(3) the structure of β-$Ni_2P_2O_7$ containing very well-distributed Pt NPs inside their cages is sufficiently stable (strong "contact" between Pt NPs and P—in addition to Ni with decreased amount in overall structure after stability test—atoms) in such harsh acidic environment used in the present work because it was able to support stationary stability tests (not tilted GC modified with β-$Ni_2P_2O_7$/Pt electrode in relation to the electrochemical cell) involving reasonable current densities. After stability tests the β-$Ni_2P_2O_7$/Pt electrode presented the lower R_{ct} value, meaning very fast charge transfer from the modified electrode to H_2 production.

■ CONCLUSIONS

In summary, hierarchically structured $Ni_3(PO_4)_2$ was synthesized by two different synthetic routes, namely, simple cost-effective precipitation and solution combustion processes, and β-$Ni_2P_2O_7$ by precipitation method. Using these as precursors, nickel pyrophosphate and nickel phosphate/Pt composites ($Ni_3(PO_4)_2$/Pt, $Ni_3(PO_4)_2'$/Pt and β-$Ni_2P_2O_7$/Pt) were prepared by using potassium hexachloroplatinate and ascorbic acid. The developed nickel pyrophosphate and nickel phosphate/Pt materials were employed as a low-cost advanced electrocatalysts for HER by water splitting. The structure purity and surface morphology of the samples were exposed by different analytical techniques such as XRD, FE-SEM, TEM, HR-TEM, electron diffraction pattern, HAADF-STEM, EDX

DOI: 10.1021/acsami.8b18153
ACS Appl. Mater. Interfaces 2019, 11, 4969−4982

mapping images, EELS, FT-IR, XPS, ICP-OES, and EIS analyses. The complete electrochemical studies exposed that the β-$Ni_2P_2O_7$/Pt electrocatalyst exhibited an excellent electrocatalytic activity for HER in acidic solution than the other samples with an overpotential of 28 mV at −10 mA·cm^{-2}, a Tafel slope of 32 mV·dec^{-1}, an j_0 of −1.31 mA·cm^{-2}, and TOF values of 1461 and 500 s^{-1} based on ECSA obtained from Cu_{upd} stripping and C_{dl}, respectively, at an overpotential of 100 mV. Moreover, the β-$Ni_2P_2O_7$/Pt electrocatalyst sustains a good stability for over 10,000 cycles or −0.1 V versus RHE for 12 days. The present investigation demonstrates that the β-$Ni_2P_2O_7$/Pt material could be a promising cost-effective electrocatalyst for H_2 production.

■ ASSOCIATED CONTENT

Supporting Information

The Supporting Information is available free of charge on the ACS Publications website at DOI: 10.1021/acsami.8b18153.

Experimental details, scheme, figures, equations, and tables concerning supplementary results and references (PDF)

■ AUTHOR INFORMATION

Corresponding Author

*E-mail: gilberto.maia@ufms.br. Tel.: +55 67 3345 3551. Fax: +55 67 3345 3552.

ORCID

Jayaraman Theerthagiri: 0000-0002-5746-5541
Jagannathan Madhavan: 0000-0003-4005-4604
Gilberto Maia: 0000-0003-2449-0887

Author Contributions

†These authors contributed equally to this work.

Author Contributions

The manuscript was written through contributions of all authors. All authors have given approval to the final version of the manuscript.

Notes

The authors declare no competing financial interest.

■ ACKNOWLEDGMENTS

G.M. wishes to thank the LME-IQSC-USP-São Carlos for the TEM facilities, the LABNANO/CBPF for technical support during electron microscopy EELS measurements, the LAMAS − Laboratório Multiusuário de Análise de Superfícies from UFRGS for the XPS facilities, GFQM-IQ-UNESP for the XRD facilities, and CNPq (grants 301403/2011-2, 473991/2012-8, 405695/2013-6, 303759/2014-3, and 442268/2014-9) and Fundect-MS (grants 23/200.583/2012, 23/200.735/2012, 23/200.246/2014, and 59/300.184/2016) for their financial support. E.S.F.C. thanks Fundect-MS (grant 23/200.675/2014), and G.V.F. thanks CAPES for the fellowship. This study was financed in part by the Coordenação de Aperfeiçoamento de Pessoal de Nível Superior − Brasil (CAPES) − Finance Code 001. In addition, B.S. gratefully acknowledges the DST (SERB), New Delhi, India for providing the fellowship (PDF/2015/000217).

■ REFERENCES

(1) Murthy, A. P.; Theerthagiri, J.; Madhavan, J.; Murugan, K. Highly Active MoS_2/Carbon Electrocatalysts for the Hydrogen Evolution Reaction − Insight into the Effect of the Internal Resistance and Roughness Factor on the Tafel Slope. *Phys. Chem. Chem. Phys.* **2017**, *19*, 1988−1998.

(2) Theerthagiri, J.; Sudha, R.; Premnath, K.; Arunachalam, P.; Madhavan, J.; Al-Mayouf, A. M. Growth of Iron Diselenide Nanorods on Graphene Oxide Nanosheets as Advanced Electrocatalyst for Hydrogen Evolution Reaction. *Int. J. Hydrogen Energy* **2017**, *42*, 13020−13030.

(3) Theerthagiri, J.; Senthil, R. A.; Senthilkumar, B.; Polu, A. R.; Madhavan, J.; Ashokkumar, M. Recent Advances in MoS_2 Nanostructured Materials for Energy and Environmental Applications − A Review. *J. Solid State Chem.* **2017**, *252*, 43−71.

(4) Li, X.; Ci, S.; Jia, J.; Wen, Z. Graphene Loading Molybdenum Carbide/Oxide Hybrids as Advanced Electrocatalysts for Hydrogen Evolution Reaction. *Int. J. Hydrogen Energy* **2016**, *41*, 21246−21250.

(5) Guo, B.; Yu, K.; Li, H.; Song, H.; Zhang, Y.; Lei, X.; Fu, H.; Tan, Y.; Zhu, Z. Hollow Structured Micro/Nano MoS_2 Spheres for Highly Electrocatalytic Activity Hydrogen Evolution Reaction. *ACS Appl. Mater. Interfaces* **2016**, *8*, 5517−5525.

(6) Hou, D.; Zhou, W.; Liu, X.; Zhou, K.; Xie, J.; Li, G.; Chen, S. Pt Nanoparticles/MoS_2 Nanosheets/Carbon Fibers as Efficient Catalyst for the Hydrogen Evolution Reaction. *Electrochim. Acta* **2015**, *166*, 26−31.

(7) Dai, X.; Li, Z.; Du, K.; Sun, H.; Yang, Y.; Zhang, X.; Ma, X.; Wang, J. Facile Synthesis of In−Situ Nitrogenated Graphene Decorated by Few−Layer MoS_2 for Hydrogen Evolution Reaction. *Electrochim. Acta* **2015**, *171*, 72−80.

(8) Chen, Y-q.; Zhang, J-f.; Wan, L.; Hu, W.-b.; Liu, L.; Zhong, C.; Deng, Y.-d. Effect of Nickel Phosphide Nanoparticles Crystallization on Hydrogen Evolution Reaction Catalytic Performance. *Trans. Nonferrous Met. Soc. China* **2017**, *27*, 369−376.

(9) Fang, Z.; Wang, Y.; Zou, Y.; Hao, Z.; Dong, Q. One-Pot Synthesis of Nickel Sulfide with Sulfur Powder as Sulfur Source in Solution and Their Electrochemical Properties for Hydrogen Evolution Reaction. *Inorg. Chem. Commun.* **2017**, *79*, 1−4.

(10) Gao, Z.; Qi, J.; Chen, M.; Zhang, W.; Cao, R. An Electrodeposited NiSe for Electrocatalytic Hydrogen and Oxygen Evolution Reactions in Alkaline Solution. *Electrochim. Acta* **2017**, *224*, 412−418.

(11) Zhang, Y.; Zang, J.; Jia, S.; Tian, P.; Han, C.; Wang, Y. Low Content of Pt Supported on Ni-MoC_x/Carbon Black as a Highly Durable and Active Electrocatalyst for Methanol Oxidation, Oxygen Reduction and Hydrogen Evolution Reactions in Acidic Condition. *Appl. Surf. Sci.* **2017**, *412*, 327−334.

(12) Deng, Z.; Wang, J.; Nie, Y.; Wei, Z. Tuning the Interface of Ni@$Ni(OH)_2$/Pd/rGO Catalyst to Enhance Hydrogen Evolution Activity and Stability. *J. Power Sources* **2017**, *352*, 26−33.

(13) Ashassi-Sorkhabi, H.; Rezaei-Moghadam, B.; Asghari, E.; Bagheri, R.; Hosseinpour, Z. Fabrication of Bridge Like Pt@MWCNTs/CoS_2 Electrocatalyst on Conductive Polymer Matrix for Electrochemical Hydrogen Evolution. *Chem. Eng. J.* **2017**, *308*, 275−288.

(14) Anantharaj, S.; Karthik, P. E.; Subramanian, B.; Kundu, S. Pt Nanoparticles Anchored Molecular Self-assemblies of DNA: An Extremely Stable and Efficient HER Electrocatalyst with Ultralow Pt Content. *ACS Catal.* **2016**, *6*, 4660−4672.

(15) Wang, L.; Zhu, Y.; Zeng, Z.; Lin, C.; Giroux, M.; Jiang, L.; Han, Y.; Greeley, J.; Wang, C.; Jin, J. Platinum-Nickel Hydroxide Nanocomposites for Electrocatalytic Reduction of Water. *Nano Energy* **2017**, *31*, 456−461.

(16) Kemppainen, E.; Bodin, A.; Sebok, B.; Pedersen, T.; Seger, B.; Mei, B.; Bae, D; Vesborg, P. C. K.; Halme, J.; Hansen, O.; Lund, P. D.; Chorkendorff, I. Scalability and Feasibility of Photoelectrochemical H_2 Evolution: The Ultimate Limit of Pt Nanoparticle as an HER Catalyst. *Energy Environ. Sci.* **2015**, *8*, 2991−2999.

(17) Wang, L.; Lin, C.; Huang, D.; Chen, J.; Jiang, L.; Wang, M.; Chi, L.; Shi, L.; Jin, J. Optimizing the Volmer Step by Single-Layer Nickel Hydroxide Nanosheets in Hydrogen Evolution Reaction of Platinum. *ACS Catal.* **2015**, *5*, 3801−3806.

DOI: 10.1021/acsami.8b18153
ACS Appl. Mater. Interfaces 2019, 11, 4969−4982

(18) Zheng, J. Seawater Splitting for High-Efficiency Hydrogen Evolution by Alloyed $PtNi_x$ Electrocatalysts. *Appl. Surf. Sci.* **2017**, *413*, 360−365.
(19) Zhou, W.; Jia, J.; Lu, J.; Yang, L.; Hou, D.; Li, G.; Chen, S. Recent Developments of Carbon-Based Electrocatalysts for Hydrogen Evolution Reaction. *Nano Energy* **2016**, *28*, 29−43.
(20) Chakrabartty, S.; Gopinath, C. S.; Raj, C. R. Polymer-Based Hybrid Catalyst of Low Pt Content for Electrochemical Hydrogen Evolution. *Int. J. Hydrogen Energy* **2017**, *42*, 22821−22829.
(21) Nazir, R.; Fageria, P.; Basu, M.; Pande, S. Decoration of Carbon Nitride Surface with Bimetallic Nanoparticles (Ag/Pt, Ag/Pd, and Ag/Au) via Galvanic Exchange for Hydrogen Evolution Reaction. *J. Phys. Chem. C* **2017**, *121*, 19548−19558.
(22) Devadas, B.; Imae, T. Hydrogen Evolution Reaction Efficiency by Low Loading of Platinum Nanoparticles Protected by Dendrimers on Carbon Materials. *Electrochem. Commun.* **2016**, *72*, 135−139.
(23) Wu, M.; Shen, P. K.; Wei, Z.; Song, S.; Nie, M. High Activity PtPd-WC/C Electrocatalyst for Hydrogen Evolution Reaction. *J. Power Sources* **2007**, *166*, 310−316.
(24) Chen, J.; Yang, Y.; Su, J.; Jiang, P.; Xia, G.; Chen, Q. Enhanced Activity for Hydrogen Evolution Reaction over CoFe Catalysts by Alloying with Small Amount of Pt. *ACS Appl. Mater. Interfaces* **2017**, *9*, 3596−3601.
(25) Kavian, R.; Choi, S.-I.; Park, J.; Liu, T.; Peng, H.-C.; Lu, N.; Wang, J.; Kim, M. J.; Xia, Y.; Lee, S. W. Pt−Ni Octahedral Nanocrystals as a Class of Highly Active Electrocatalysts Toward the Hydrogen Evolution Reaction in an Alkaline Electrolyte. *J. Mater. Chem. A* **2016**, *4*, 12392−12397.
(26) Wang, S.; Yang, G.; Yang, S. Pt-Frame@Ni *quasi* Core−Shell Concave Octahedral $PtNi_3$ Bimetallic Nanocrystals for Electrocatalytic Methanol Oxidation and Hydrogen Evolution. *J. Phys. Chem. C* **2015**, *119*, 27938−27945.
(27) Luo, Y.; Huang, D.; Li, M.; Xiao, X.; Shi, W.; Wang, M.; Su, J.; Shen, Y. MoS_2 Nanosheet Decorated with Trace Loads of Pt as Highly Active Electrocatalyst for Hydrogen Evolution Reaction. *Electrochim. Acta* **2016**, *219*, 187−193.
(28) Deng, J.; Li, H.; Xiao, J.; Tu, Y.; Deng, D.; Yang, H.; Tian, H.; Li, J.; Ren, P.; Bao, X. Triggering the Electrocatalytic Hydrogen Evolution Activity of the Inert Two-Dimensional MoS_2 Surface via Single-Atom Metal Doping. *Energy Environ. Sci.* **2015**, *8*, 1594−1601.
(29) Bai, S.; Wang, C.; Deng, M.; Gong, M.; Bai, Y.; Jiang, J.; Xiong, Y. Surface Polarization Matters: Enhancing the Hydrogen-Evolution Reaction by Shrinking Pt Shells in Pt−Pd−Graphene Stack Structures. *Angew. Chem., Int. Ed.* **2014**, *53*, 12120−12124.
(30) Yin, J.; Fan, Q.; Li, Y.; Cheng, F.; Zhou, P.; Xi, P.; Sun, S. Ni−C−N Nanosheets as Catalyst for Hydrogen Evolution Reaction. *J. Am. Chem. Soc.* **2016**, *138*, 14546−14549.
(31) Rowley-Neale, S. J.; Brownson, D. A. C.; Smith, G. C.; Sawtell, D. A. G.; Kelly, P. J.; Banks, C. E. 2D Nanosheet Molybdenum Disulphide (MoS_2) Modified Electrodes Explored Towards the Hydrogen Evolution Reaction. *Nanoscale* **2015**, *7*, 18152−18168.
(32) Senthilkumar, B.; Khan, Z.; Park, S.; Kim, K.; Ko, H.; Kim, Y. Highly Porous Graphitic Carbon and $Ni_2P_2O_7$ for a High Performance Aqueous Hybrid Supercapacitor. *J. Mater. Chem. A* **2015**, *3*, 21553−21561.
(33) de Lima, F.; Maia, G. Oxidized/Reduced Graphene Nanoribbons Facilitate Charge Transfer to the $Fe(CN)_6^{3-}/Fe(CN)_6^{4-}$ Redox Couple and towards Oxygen Reduction. *Nanoscale* **2015**, *7*, 6193−6207.
(34) Chen, D.; Tao, Q.; Liao, L. W.; Liu, S. X.; Chen, Y. X.; Ye, S. Determining the Active Surface Area for Various Platinum Electrodes. *Electrocatalysis* **2011**, *2*, 207−219.
(35) Green, C. L.; Kucernak, A. Determination of the Platinum and Ruthenium Surface Areas in Platinum−Ruthenium Alloy Electrocatalysts by Underpotential Deposition of Copper. I. Unsupported Catalysts. *J. Phys. Chem. B* **2002**, *106*, 1036−1047.
(36) Angerstein-Kozlowska, H. Surfaces, Cells, and Solutions for Kinetic Studies. In *Comprehensive Treatise of Electrochemistry*; Yearger, E., Bockris, J. O'M., Conway, B. E., Sarangapani, S., Eds.; Plenum Press: New York, 1984; Vol. *9*, Chapter 2, pp 15−59.
(37) McCrory, C. C. L.; Jung, S.; Peters, J. C.; Jaramillo, T. F. Benchmarking Heterogeneous Electrocatalysts for the Oxygen Evolution Reaction. *J. Am. Chem. Soc.* **2013**, *135*, 16977−16987.
(38) Jayaraman, T.; Raja, S. A.; Priya, A.; Jagannathan, M.; Ashokkumar, M. Synthesis of a Visible-Light Active V_2O_5−g-C_3N_4 Heterojunction as an Efficient Photocatalytic and Photoelectrochemical Material. *New J. Chem.* **2015**, *39*, 1367−1374.
(39) Theerthagiri, J.; Senthil, R. A.; Priya, A.; Madhavan, J.; Michael, R. J. V.; Ashokkumar, M. Photocatalytic and Photoelectrochemical Studies of Visible-Light Active α-Fe_2O_3−g-C_3N_4 Nanocomposites. *RSC Adv.* **2014**, *4*, 38222−38229.
(40) Theerthagiri, J.; Senthil, R. A.; Arunachalam, P.; Madhavan, J.; Buraidah, M. H.; Amutha, S.; Arof, A. K. Synthesis of Various Carbon Incorporated Flower-Like MoS_2 Microspheres as Counter Electrode for Dye-Sensitized Solar Cells. *J. Solid State Electrochem.* **2017**, *21*, 581−590.
(41) Theerthagiri, J.; Thiagarajan, K.; Senthilkumar, B.; Khan, Z.; Senthil, R. A.; Arunachalam, P.; Madhavan, J.; Ashokkumar, M. Synthesis of Hierarchical Cobalt Phosphate Nanoflakes and Their Enhanced Electrochemical Performances for Supercapacitor Applications. *ChemistrySelect* **2017**, *2*, 201−210.
(42) Theerthagiri, J.; Senthil, R. A.; Buraidah, M. H.; Raghavender, M.; Madhavan, J.; Arof, A. K. Synthesis and Characterization of $(Ni_{1-x}Co_x)Se_2$ Based Ternary Selenides as Electrocatalyst for Triiodide Reduction in Dye-Sensitized Solar Cells. *J. Solid State Chem.* **2016**, *238*, 113−120.
(43) Venarusso, L. B.; Bettini, J.; Maia, G. Superior Catalysts for Oxygen Reduction Reaction Based on Porous Nanostars of a Pt, Pd, or Pt−Pd Alloy Shell Supported on a Gold Core. *ChemElectroChem* **2016**, *3*, 749−756.
(44) Venarusso, L. B.; Bettini, J.; Maia, G. Catalysts for Oxygen Reduction Reaction Based on Nanocrystals of a Pt or Pt−Pd Alloy Shell Supported on a Au Core. *J. Solid State Electrochem.* **2016**, *20*, 1753−1764.
(45) Fortunato, G. V.; de Lima, F.; Maia, G. Oxygen-Reduction Reaction Strongly Electrocatalyzed by Pt Electrodeposited onto Graphene or Graphene Nanoribbons. *J. Power Sources* **2016**, *302*, 247−258.
(46) Boone, C. V.; Maia, G. Pt−Pd and Pt−Pd−(Cu or Fe or Co)/Graphene Nanoribbon Nanocomposites as Efficient Catalysts Toward the Oxygen Reduction Reaction. *Electrochim. Acta* **2017**, *247*, 19−29.
(47) Venarusso, L. B.; Boone, C. V.; Bettini, J.; Maia, G. Carbon-Supported Metal Nanodendrites as Efficient, Stable Catalysts for the Oxygen Reduction Reaction. *J. Mater. Chem. A* **2018**, *6*, 1714−1726.
(48) Koyama, Y.; Mizoguchi, T.; Ikeno, H.; Tanaka, I. Electronic Structure of Lithium Nickel Oxides by Electron Energy Loss Spectroscopy. *J. Phys. Chem. B* **2005**, *109*, 10749−10755.
(49) Keast, V. J.; Scott, A. J.; Brydson, R.; Williams, D. B.; Bruley, J. Electron Energy-Loss Near-Edge Structure − A Tool for the Investigation of Electronic Structure on the Nanometre Scale. *J. Microsc.* **2001**, *203*, 135−175.
(50) Favron, A.; Gaufrès, E.; Fossard, F.; Phaneuf-L'Heureux, A.-L.; Tang, N. Y-W.; Lévesque, P. L.; Loiseau, A.; Leonelli, R.; Francoeur, S.; Martel, R. Photooxidation and Quantum Confinement Effects in Exfoliated Black Phosphorus. *Nat. Mater.* **2015**, *14*, 826−832.
(51) Wu, R. J.; Topsakal, M.; Low, T.; Robbins, M. C.; Haratipour, N.; Jeong, J. S.; Wentzcovitch, R. M.; Koester, S. J.; Mkhoyan, K. A. Atomic and Electronic Structure of Exfoliated Black Phosphorus. *J. Vac. Sci. Technol. A* **2015**, *33*, 060604.
(52) Wulan, B.-R.; Yi, S.-S.; Li, S.-J.; Duan, Y.-X.; Yan, J.-M.; Jiang, Q. Amorphous Nickel Pyrophosphate Modified Graphitic Carbon Nitride: An Efficient Photocatalyst for Hydrogen Generation from Water Splitting. *Appl. Catal., B* **2018**, *231*, 43−50.
(53) Sankar, K. V.; Seo, Y.; Lee, S. C.; Jun, S. C. Redox Additive-Improved Electrochemically and Structurally Robust Binder-Free Nickel Pyrophosphate Nanorods as Superior Cathode for Hybrid Supercapacitors. *ACS Appl. Mater. Interfaces* **2018**, *10*, 8045−8056.

DOI: 10.1021/acsami.8b18153
ACS Appl. Mater. Interfaces 2019, 11, 4969−4982

(54) Chen, C.; Zhang, N.; He, Y.; Liang, B.; Ma, R.; Liu, X. Controllable Fabrication of Amorphous Co—Ni Pyrophosphates for Tuning Electrochemical Performance in Supercapacitors. *ACS Appl. Mater. Interfaces* **2016**, *8*, 23114−23121.
(55) Zhang, N.; Chen, C.; Chen, Y.; Chen, G.; Liao, C.; Liang, B.; Zhang, J.; Li, A.; Yang, B.; Zheng, Z.; Liu, X.; Pan, A.; Liang, S.; Ma, R. $Ni_2P_2O_7$ Nanoarrays with Decorated C_3N_4 Nanosheets as Efficient Electrode for Supercapacitors. *ACS Appl. Energy Mater.* **2018**, *1*, 2016−2023.
(56) Zheng, J.; Yan, Y.; Xu, B. Correcting the Hydrogen Diffusion Limitation in Rotating Disk Electrode Measurements of Hydrogen Evolution Reaction Kinetics. *J. Electrochem. Soc.* **2015**, *162*, F1470−F1481.
(57) Chen, J. G.; Jones, C. W.; Linic, S.; Stamenkovic, V. R. Best Practices in Pursuit of Topics in Heterogeneous Electrocatalysis. *ACS Catal.* **2017**, *7*, 6392−6393.
(58) Chen, R.; Yang, C.; Cai, W.; Wang, H.-Y.; Miao, J.; Zhang, L.; Chen, S.; Liu, B. Use of Platinum as the Counter Electrode to Study the Activity of Nonprecious Metal Catalysts for the Hydrogen Evolution Reaction. *ACS Energy Lett.* **2017**, *2*, 1070−1075.
(59) Wei, R.; Fang, M.; Dong, G.; Ho, J. C. Is Platinum a Suitable Counter Electrode Material for Electrochemical Hydrogen Evolution Reaction? *Sci. Bull.* **2017**, *62*, 971−973.
(60) Neyerlin, K. C.; Gu, W.; Jorne, J.; Gasteiger, H. A. Study Of The Exchange Current Density for the Hydrogen Oxidation and Evolution Reactions. *J. Electrochem. Soc.* **2007**, *154*, B631−B635.
(61) Meguerdichian, A. G.; Jafari, T.; Shakil, M. R.; Miao, R.; Achola, L. A.; Macharia, J.; Shirazi-Amin, A.; Suib, S. L. Synthesis and Electrocatalytic Activity of Ammonium Nickel Phosphate, $[NH_4]$-$NiPO_4{\cdot}6H_2O$, and β-Nickel Pyrophosphate, β-$Ni_2P_2O_7$: Catalysts for Electrocatalytic Decomposition of Urea. *Inorg. Chem.* **2018**, *57*, 1815−1823.
(62) Li, K.; Li, Y.; Wang, Y.; Ge, J.; Liu, C.; Xing, W. Enhanced Electrocatalytic Performance for the Hydrogen Evolution Reaction Through Surface Enrichment of Platinum Nanoclusters Alloying with Ruthenium in Situ Embedded in Carbon. *Energy Environ. Sci.* **2018**, *11*, 1232−1239.
(63) Ji, S.; Yang, Z.; Zhang, C.; Liu, Z.; Tjiu, W. W.; Phang, I. Y.; Zhang, Z.; Pan, J.; Liu, T. Exfoliated MoS_2 Nanosheets as Efficient Catalysts for Electrochemical Hydrogen Evolution. *Electrochim. Acta* **2013**, *109*, 269−275.
(64) Pu, Z.; Liu, Q.; Asiri, A. M.; Luo, Y.; Sun, X.; He, Y. 3D Macroporous MoS_2 Thin Film: In Situ Hydrothermal Preparation and Application as a Highly Active Hydrogen Evolution Electrocatalyst at All pH Values. *Electrochim. Acta* **2015**, *168*, 133−138.
(65) Vesborg, P. C. K.; Seger, B.; Chorkendorff, I. Recent Development in Hydrogen Evolution Reaction Catalysts and Their Practical Implementation. *J. Phys. Chem. Lett.* **2015**, *6*, 951−957.
(66) Trasatti, S. Work Function, Electronegativity, and Electrochemical Behaviour of Metals: III. Electrolytic Hydrogen Evolution in Acid Solutions. *J. Electroanal. Chem. Interfacial Electrochem.* **1972**, *39*, 163−184.
(67) Zou, X.; Zhang, Y. Noble Metal-Free Hydrogen Evolution Catalysts for Water Splitting. *Chem. Soc. Rev.* **2015**, *44*, 5148−5180.

DOI: 10.1021/acsami.8b18153
ACS Appl. Mater. Interfaces 2019, 11, 4969−4982